Numerical investigation of gaseous cellular detonation propagation in rough-walled channels

Yifan Lyu

A Thesis

in

The Department

of

Mechanical, Industrial and Aerospace Engineering

Presented in Partial Fulfillment of the Requirements

for the Degree of

Master of Applied Science (Mechanical Engineering) at

Concordia University

Montréal, Québec, Canada

March 2023

CONCORDIA UNIVERSITY

School of Graduate Studies

This is to certify that the thesis prepared

By: **Yifan Lyu**

Entitled: **Numerical investigation of gaseous cellular detonation propagation in rough-walled channels**

and submitted in partial fulfillment of the requirements for the degree of

Master of Applied Science (Mechanical Engineering)

complies with the regulations of this University and meets the accepted standards with respect to originality and quality.

Signed by the Final Examining Committee:

_____ Chair
Dr. Lyes Kadem

_____ External Examiner
Dr. Ebenezer Ekow Essel

_____ Examiner
Dr. Lyes Kadem

_____ Supervisor
Dr. Hoi Dick Ng

Approved by _____
Dr. Sivakumar Narayanswamy, Graduate Program Director
Department of Mechanical, Industrial and Aerospace Engineering

_____ 2023

_____
Dr. Mourad Debbabi, Dean
Gina Cody School of Engineering and Computer Science

Abstract

Numerical investigation of gaseous cellular detonation propagation in rough-walled channels

Yifan Lyu

When a cellular detonation propagates in a tube with rough-wall boundary conditions, its propagating velocity becomes less than the ideal Chapman-Jouguet (CJ) value due to losses. In addition, the intrinsic cellular pattern of this quasi-detonation and its reacting flow fields can be strongly changed by the presence of wall roughness. This study aims to clarify the wall boundary effect by investigating the quasi-detonations under different degrees of wall roughness defined by various characteristic factors. A computational analysis is conducted using two-dimensional numerical simulations. The governing equations are given by the reactive Euler equations with a two-step Arrhenius induction-reaction kinetic model and solved numerically using a second order finite-volume scheme with Graphics Processing Unit (GPU) computing. A parametric study is reported by varying the channel width, obstacle size, obstacle spacing and chemical reaction parameters, to investigate perturbations created by the rough wall to the intrinsic cellular detonation instability and eventually the detonation failure or propagation limit. Apart from the numerical smoked foils to reveal the dynamic evolution and irregularity of cellular detonation patterns, the degree of instabilities caused by the roughness is analyzed by looking at the probability density function of the pressure and induction rate from the detonation flow fields.

Acknowledgments

First and foremost, I would like to express deep gratitude to my supervisor, Prof. Hoi Dick Ng, for his guidance with patience, understanding, and tolerance throughout my graduate studies. His comprehensive understanding of detonation and even the entire field of thermodynamics not only helped me sort out my research ideas but also put forward many valuable suggestions. It is because of his existence that I was able to complete this article in a short time.

This work could not have been completed without the help of many people. I would like to thank Chian Yan for helping me with a primary understanding of the field of detonation and combustion and guiding me in programming learning. I also want to thank several other students in the laboratory, George, Sean, and Ting. With their company, my oral English ability has improved a lot, and my daily communication with them has also made my academic thinking ability more complete.

Finally, I want to extend my full gratitude to my family, who is very supportive of the choices I made. Without them, I would not have completed this article.

Contents

List of Figures vii

List of Tables xi

Glossary xii

1 Introduction 1

1.1 Motivation . . . 1

1.2 Fundamentals of detonations . . . 2

1.2.1 Chapman-Jouguet theory . . . 2

1.2.2 One-dimensional steady detonation model . . . 2

1.2.3 Unstable cellular detonation structure . . . 4

1.3 Limits and near-limit behavior of detonation . . . 5

1.4 Near-limit gaseous detonations in roughed-wall tubes . . . 6

1.5 Objective of the thesis . . . 8

1.6 Thesis outline . . . 9

1.7 Contribution to knowledge . . . 9

2 Formulations and Methods 10

2.1 Governing equations . . . 10

2.2 Numerical methods . . . 14

2.2.1 Operator splitting . . . 14

2.2.2 Riemann problem and Godunov's method . . . 15

2.2.3 HLLC approximate Riemann solver . . . 18
2.2.4 MUSCL-Hancock scheme . . . 22
2.2.5 TVD of MUSCL-Hancock scheme . . . 25
2.3 Computational time steps . . . 27
2.4 CUDA . . . 28
2.5 Code validation . . . 29
2.5.1 One-dimensional Sod shock tube problem . . . 29
2.5.2 Two-dimensional structure of cellular detonation . . . 30
2.6 Grid resolution study . . . 33
2.7 Summary . . . 34

3 Parametric Study of Roughness Effects Induced by Obstacles 35
3.1 Computational setup . . . 36
3.2 Comparison between smooth and rough channels . . . 37
3.3 Effect of different widths in smooth and rough tubes . . . 39
3.4 Effect of the rate constant of heat release k_R . . . 40
3.5 Effect of roughness factor n . . . 42
3.6 Effect of length between two obstacles l . . . 44
3.7 Effect of different initial conditions . . . 46

4 Comparison between Staggered and Aligned Obstacle Configurations 48
4.1 Computational setup . . . 48
4.2 Soot foil comparison . . . 49
4.3 Velocity comparison . . . 50
4.4 Probability density function comparison . . . 54

5 Conclusions 57

Bibliography 58

List of Figures

Figure 1.1 p-V diagram and the Chapman-Jouguet condition. Results obtained with Q = 21.365, γ = 1.32, the Chapman-Jouguet Mach number is M_{CJ} = 5.0984. 3

Figure 1.2 One-dimensional ZND model of the steady detonation structure. 4

Figure 1.3 A schlieren image (a) as well its soot foil (b) for a weakly unstable, detonation: $2\mathrm{H}_2 - \mathrm{O}_2 - 12\mathrm{Ar}$ (Austin, 2003). 4

Figure 1.4 Experimental smoked foil records for different types of a combustible mixture (Voitsekhovskii, Kotov, Mitrofanov, and Topchiyan, 1958) 5

Figure 2.1 Geometrical illustration of the finite volume update formula. 16

Figure 2.2 Control volume $[x_{\mathrm{L}}, x_{\mathrm{R}}] \times [0, T]$ on x-t plane. $\mathbf{S}_{\mathrm{L}}$ and $\mathbf{S}_{\mathrm{R}}$ are the fastest signal velocities arising from the solution of the Riemann problem. 18

Figure 2.3 Waves structure of the exact solution $\mathbf{U}_{i+\frac{1}{2}}(x/t)$ of the Riemann Problem for the one-dimensional Euler equations. 19

Figure 2.4 HLLC approximate Riemann solver. The solution in the star region consists of two constant states separated from each other by a middle wave of speed $\mathbf{S}_*$. . . 19

Figure 2.5 Piece-wise linear MUSCL reconstruction of data in a single computing cell I_i, boundary extrapolated values are u_i^{L}, u_i^{R}. 23

Figure 2.6 Piece-wise linear MUSCL reconstruction for three successive computing cells I_{i-1}, I_i, I_{i+1}. 23

Figure 2.7 Piecewise linear data. 24

Figure 2.8 Structure of the solution in x–t plane. 24

Figure 2.9 TVD region for slope limiters. For negative r, TVD region is single line ε = 0 and for positive r, TVD region lies between 0 and $min\left(\varepsilon_{\mathrm{L}}\left(r\right),\ \varepsilon_{\mathrm{R}}(r)\right)$. 26
Figure 2.10 Implementation of the Riemann solver using the thread and block configuration with a one-cell overlap between blocks (Morgan, 2013). 28
Figure 2.11 Velocity, pressure, and energy plots for exact and approximate solution of Sod's shock tube problem. 29
Figure 2.12 The initial and boundary conditions of the simulation. 30
Figure 2.13 Numerical soot foil of $E_{\mathrm{a}} = 10$. The upper figure is the result of early time showing the sinusoidal perturbation and the initiation of detonation; the lower one is the late cellular structure. 32
Figure 2.14 Numerical soot foil of $E_{\mathrm{a}} = 20$ at late times, of which the cellular structure becomes irregular. 32
Figure 2.15 Numerical soot foil of $E_{\mathrm{a}} = 25$ at late times, of which the cellular structure is more chaotic. 32
Figure 2.16 A sequence of four density schlieren plots of detonation structure development with $E_{\mathrm{a}} = 20$. 33
Figure 2.17 Numerical soot foils showing the cellular detonation structure and average cell size γ in a smooth channel obtained with a resolution of 10 (left) and 20 (right) grid points per unit $L_{1/2}$. 33
Figure 3.1 Schematic of an incident detonation wave propagating into a rough-walled channel and the computational domain (red dashed box). 36
Figure 3.2 Smooth and rough-walled tube models. 38
Figure 3.3 Soot foils showing cellular patterns of detonations in a smooth channel with $D_{1/2} = 300$ and $k_{\mathrm{R}} = 1$ in the upper figure, the below one is the quasi-detonation with obstacle height $n = 1$. 38
Figure 3.4 Time-dependent transient velocity evolution (blue line) when $k_{\mathrm{R}} = 1$ and average velocity in a smooth tube as well as propagating in rough-walled channels with obstacle height $n = 1$. 38

Figure 3.5 Soot foils showing cellular patterns of CJ detonations at $k_{\mathrm{R}} = 4$ in smooth channels with different half channel widths: (a) $D_{1/2} = 200$ and (b) $D_{1/2} = 300$. . 39

Figure 3.6 Soot foils showing cellular patterns of quasi-detonations at $k_{\mathrm{R}} = 4$ in rough-walled channels with obstacle size $n = 1$: (a) $D_{1/2} = 200$ and (b) $D_{1/2} = 300$. . . 39

Figure 3.7 A sample numerical soot foil showing the computational setup and the cellular detonation pattern in a rough-walled channel. 40

Figure 3.8 Soot foils showing cellular patterns of quasi-detonations in rough-walled channels with $D_{1/2} = 300$, obstacle height $n = 1$, and (a) $k_R = 1$, (b) $k_{\mathrm{R}} = 2$ and (c) $k_{\mathrm{R}} = 4$. The dash-lined boxes display the incident CJ detonation patterns. . . . 41

Figure 3.9 The average velocity ratio V/V_{CJ} within a given time range (from 0 to 2000) with a grid of resolution 10 points per unit $L_{1/2}$, domain 400×300, with different pre-exponential factors k_{R} and different roughness factors n (obstacle size): (a): $k_{\mathrm{R}} = 1, n = 1$ (obstacle 25×25); (b): $k_{\mathrm{R}} = 2, n = 1$; and (c): $k_{\mathrm{R}} = 4, n = 1$. . . 41

Figure 3.10 Soot foils showing cellular patterns of detonations in channels with $D_{1/2} = 300$ and $k_{\mathrm{R}} = 4$, (a) smooth channel, (b) $n = 1$, (c) $n = 2$ and (d) $n = 3$. 42

Figure 3.11 The relationship between average velocity and roughness factors n of detonation propagation in channels with $D_{1/2} = 300$ and heat release constant $k_{\mathrm{R}} = 1, 2, 4$. (Ignoring the smooth part causing their average velocity to be approximately V_{CJ}, makes $V/V_{\mathrm{CJ}} = 1$) 43

Figure 3.12 Left part is the average velocity ratio V/V_{CJ} within a given time range (from 0 to 1200) with a grid of resolution 10 points per unit $L_{1/2}$, domain 400×300, with different roughness factors n; Right part is a transient frame of this relatively "steady" state shown in the density contour. 44

Figure 3.13 Soot foils showing cellular patterns of detonations in channels with $D_{1/2} = 300$, $k_{\mathrm{R}} = 1$, and $n = 1$, the length factor $l = 8, 4, 8/3$ and 2, respectively. 45

Figure 3.14 The average velocity ratio V/V_{CJ} within a given time range (from 0 to 2000) with a grid of resolution 10 points per unit $L_{1/2}$, domain 400×300, with different length factors l. 45

Figure 3.15 The relationship between average velocity and the length between two obstacles l for detonation propagation in channels with $D_{1/2} = 300$ and heat release constant $k_{\mathrm{R}} = 1, 2, 4$ and the roughness factors $n = 1, 2, 3$. 46
Figure 3.16 Time-dependent transient velocity evolution and average velocity of the quasi-detonation propagating in rough-walled channels with $n = 3$, using different incident CJ detonation waves. 47
Figure 4.1 The model of previous aligned obstacles rough wall in (I) and the model of staggered obstacles rough wall in this part in (II). 48
Figure 4.2 The soot foil of the incident detonation with the domain 600×800 and heat release constant $k_{\mathrm{R}} = 4$. 49
Figure 4.3 Soot foils showing cellular patterns of detonations in staggered obstacles with $D_{1/2} = 300$, $k_{\mathrm{R}} = 4$, and $n = 1, 2, 3, 4, 5$, respectively. 50
Figure 4.4 Soot foils showing cellular patterns of detonations in aligned obstacles with $D_{1/2} = 300$, $k_{\mathrm{R}} = 4$, and $n = 1, 2, 3, 4, 5$, respectively. 50
Figure 4.5 Time-velocity ratio graphs showing cellular patterns of detonations in channels with staggered obstacles for $D_{1/2} = 300$, $k_{\mathrm{R}} = 4$, and $n = 1, 2, 3, 4, 5$, respectively. 51
Figure 4.6 Time-velocity ratio graphs showing cellular patterns of detonations in channels with aligned obstacles for $D_{1/2} = 300$, $k_{\mathrm{R}} = 4$, and $n = 1, 2, 3, 4, 5$, respectively. 52
Figure 4.7 The relationship between average velocity and the roughness factor n of detonation propagation with $D_{1/2} = 300$ and heat release constant $k_{\mathrm{R}} = 4$ in staggered as well as aligned channels. 53
Figure 4.8 Galloping detonation period Ω over the average cell size λ for different roughness factors $n = 1, 2, 3, 4, 5$ with pre-experiential factor $k_{\mathrm{R}} = 4$ for aligned and staggered obstacles. 53
Figure 4.9 Probability density function as well as the corresponding soot foil and velocity ratio graphs for different roughness factors $n = 1, 3, 5$ with pre-experiential factor $k_{\mathrm{R}} = 4$ for staggered obstacles. 54

List of Tables

Table 2.1 Initial conditions for the cellular detonation simulation. 31

Table 3.1 Mixture parameters and corresponding CJ detonation properties. 37

Glossary

c	Courant number
c_0	Speed of sound
d	Tube diameter
D	Detonation velocity
$D_{1/2}$	Half channel width
e	Specific internal energy
E_a	Global activation energy
E_I	Activation energy of the induction process
E_R	Activation energy of the heat release process
$\mathbf{F}$	Convective flux in the x-direction
$\mathbf{G}$	Convective flux in the y-direction
H	Heaviside step function
i	The i^{th} cell
k_I	Reaction rate constant of the induction process
k_R	Reaction rate constant of the heat release process
l	Length between two obstacles
$L_{1/2}$	Half reaction zone length
L_C	Operators for the convective terms
L_S	Operators for the reactive source terms
M_CJ	Chapman-Jouguet Mach number

n	Obstacle height factor
p	Pressure
Q	Chemical energy release
r	Ratio of the slope at the surface of each cell
R	Universal gas constant
$\mathbf{S}$	Source term
$\mathbf{S}_{\mathrm{L}}$	Speed of left-going waves in Riemann Problem
$\mathbf{S}_{\mathrm{R}}$	Speed of right-going waves in Riemann Problem
$\mathbf{S}_{*}$	Speed of middle waves
t	Time
T	Temperature
T_s	Post-shock temperature
u	Particle velocity in the x-direction
u_{vn}	von Neumann velocity
$\mathbf{U}$	Conserved variable
v	Particle velocity in the y-direction
V	Volume/ Detonation velocity
V_{CJ}	Chapman-Jouguet detonation velocity
X	Distance along first coordinate direction
Y	Distance along second coordinate direction

Acronyms

BC	Boundary Conditions
BR	Blockage Ratio
CFL	Courant-Friedrichs-Lax
CJ	Chapman-Jouguet
CUDA	Compute Unified Device Architecture
DDT	Deflagration to Detonation Transition
GPGPU	General Purpose Graphics Processing Unit

GPU	Graphics Processing Unit
HLLC	Harten-Lax-van Leer Contact
IBVP	Initial-Boundary Value Problem
IC	Initial Conditions
MUSCL	Monotone Upwind Scheme for Conservation Laws
ODW	Oblique Detonation Wave
PDEs	Partial Differential Equations
PDF	Probability Density Function
RP	Riemann Problem
VN	von Neumann
ZND	Zel'dovich-von Neumann-Döring

Greek symbols

α	Obstacle width
β	Reaction progress variable
Δ_i	Slope vector in the MUSCL reconstruction
Δ_{I}	Characteristic induction zone length
Δ_{R}	Characteristic reaction zone length
Δt	A time-slope vector in an operator splitting scheme
Δx	Mesh spacing
$\varepsilon(r)$	Slope limiter
ε_{I}	Reduced activation energy of the induction process
ε_{R}	Reduced activation energy of the heat release process
γ	Ratio of specific heats
λ	Detonation cell size
$\dot{\omega}_{\mathrm{I}}$	Chemical reaction rate of the induction process
$\dot{\omega}_{\mathrm{R}}$	Chemical reaction rate of the heat release process
Ω	Galloping detonation period
π	Ratio of circumference to diameter

ρ	Density
ξ	Reaction progress variable for the induction process

Subscripts

0	Initial condition, unburnt mixture properties
L	Left
$\max$	Maximum
R	Right
ref	Reference scale

Chapter 1

Introduction

1.1 Motivation

A detonation is a supersonic, compression wave consisting of a leading shock sustained by a hydrodynamic reactive flow. Due to the violent nature of this combustion mode with a large increase in pressure and temperature, the detonation phenomenon has long been studied for explosion safety in chemical and energy industrial settings (Hirano, 2002; Nettleton, 2002; Lee, 2008; Ng and Lee, 2008).

Detonation research has focused on predicting the detonation of explosives, their ability to detonate, and the constraints that are critical to appropriate risk rates for chemical facilities, accident prevention, and transport safety of hazardous materials. More recently, there is an intensifying effort to turn the negative outcomes of detonation into positive impacts by harnessing its pressure gain for developing advanced aerospace propulsion systems to achieve potentially higher thermal efficiency (Kailasanath, 2003; Roy et al., 2004; Wola'nski, 2013; Ma et al., 2020; Rosato et al., 2021).

One of the most fundamental problems in detonation is to find out how fast the detonation wave propagates in an explosive mixture and what are the limit conditions. The detonation speed depends on both initial and boundary conditions. The initial conditions refer to the type of fuel, mixture conditions, and the initial thermodynamic states. The boundary conditions are related to the size and characteristics of the wall confinement. The wall boundaries can affect the detonation propagation dynamics and generate losses causing failure. The latter is the problem addressed in this thesis,

i.e., how does the wall roughness change the unsteady detonation structure and its dynamics, and what are the near-limit propagation behavior of the detonation under the influence of the boundary conditions?

1.2 Fundamentals of detonations

1.2.1 Chapman-Jouguet theory

The phenomenon of detonation was discovered in 1881 by four French scientists, i.e., Berthelot, Vieille, Mallard, and Le Chatelier (see the monograph by Lee (2008) for the historical background). Analytically, the first theory to predict the detonation propagation velocity was formulated by Chapman and Jouguet (Fickett & Davis, 2000), nowadays referred to as the Chapman-Jouguet (CJ) Theory. The CJ theory is a thermodynamic equilibrium analysis based on a control volume approach. The theory can be well-represented in a p-V diagram (Fig. 1.1). To compute the velocity of a normal CJ detonation (i.e., steady, planar, and one-dimensional), combining the continuity and the conservation of momentum gives the Rayleigh line, while the conservation of energy and continuity provides the Hugoniot curve which represents all the possible thermodynamic states behind the detonation wave. To close the set of governing equations, the unique detonation state can readily be determined from the CJ criterion of sonic flow behind the wave. The p-V diagram is represented by the tangency intersection point between the Rayleigh line and the product Hugoinot curve.

The CJ theory generally predicts the velocity of a normal CJ detonation propagating in a very large tube in good agreement with experiments. The CJ velocity is based on purely the energetics of the mixture and evaluated from thermodynamic equilibrium computations. It does not consider the actual structure of the detonation wave and hence, it does not lead to the dynamic parameters of a detonation wave such as limits and critical phenomena since these are all related to the detailed structure of the detonation front.

1.2.2 One-dimensional steady detonation model

The first detonation structure was formulated independently by Zel'dovich, von Neumann and Döring in the early 1940s, known as the one-dimensional steady ZND structure (Lee, 2008).

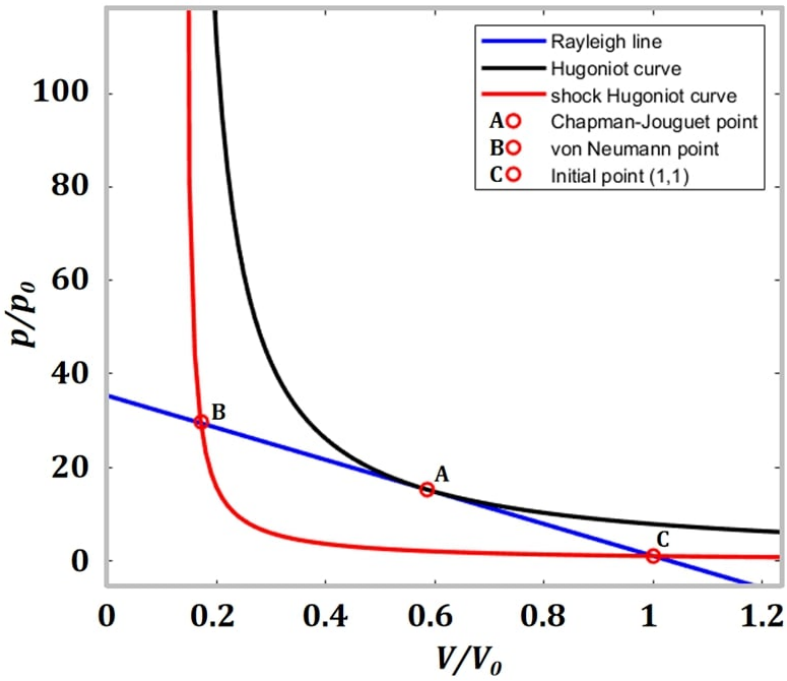

Figure 1.1: p-V diagram and the Chapman-Jouguet condition. Results obtained with Q = 21.365, γ = 1.32, the Chapman-Jouguet Mach number is M_{CJ} = 5.0984.

This classical ZND model describes detonation as a structure consisting of an inert normal shock and a chemical reaction zone. The post-shock condition (or Von Neumann state) triggers the chemical reaction, and after the thermally neutral induction zone, the exothermic chemical reaction continues. The flow in the reaction zone is subsonic. At the end of the reaction zone, the flow reaches the local speed of sound according to the Chapman-Jouguet condition. The importance of the ZND model is that it provides the underlying propagation mechanism that detonation is sustained by the work done by autoignition through the release of chemical energy from adiabatic shock compression and the expansion behind the shock front.

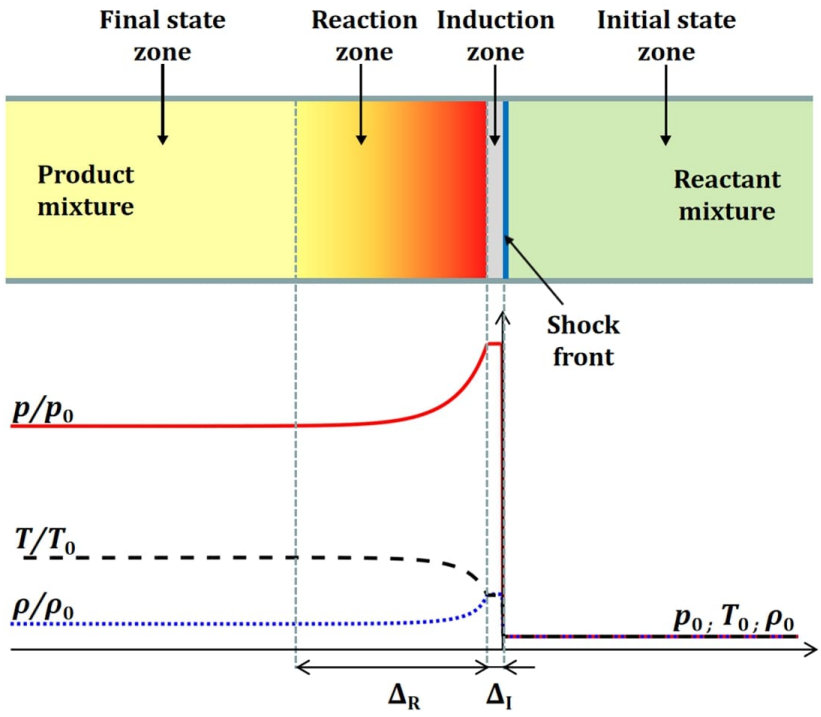

Figure 1.2: One-dimensional ZND model of the steady detonation structure.

1.2.3 Unstable cellular detonation structure

However, the ideal ZND model assumes that the detonation wave is a steady one-dimensional configuration and in fact, the structure predicted by this one-dimensional theory is seldom observed experimentally. In reality, the detonation structure in gaseous explosives is inherently unstable, having a complex flow field with various degrees of instabilities features (Shepherd, 2009). The frontal structure consists of a set of interacting shocks and hydrodynamic instabilities which form a cell-like pattern, referred to as detonation cells, see Fig. 1.3.

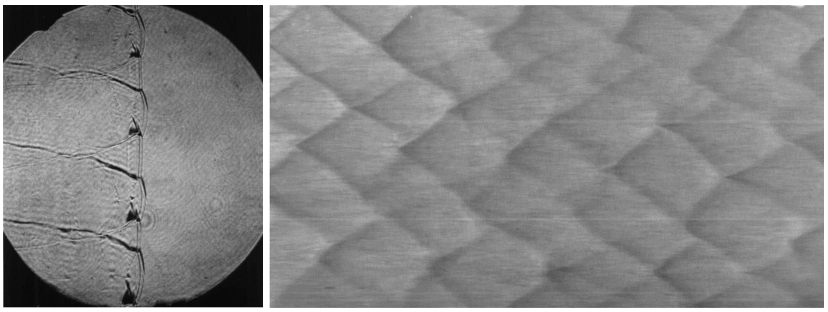

Figure 1.3: A schlieren image (a) as well its soot foil (b) for a weakly unstable, detonation: $2H_2 - O_2 - 12Ar$ (Austin, 2003).

A quantitative description of the multi-dimensional unstable cellular structure is not possible as yet. No theoretical model can reflect the real three-dimensional cellular characteristic of the detonation wave. Besides direct photographic observation as shown in Fig. 1.3, the smoked foil technique is commonly used to observe the cellular detonation pattern and to determine the characteristic cell size (see Fig. 1.3(b) and 1.4).

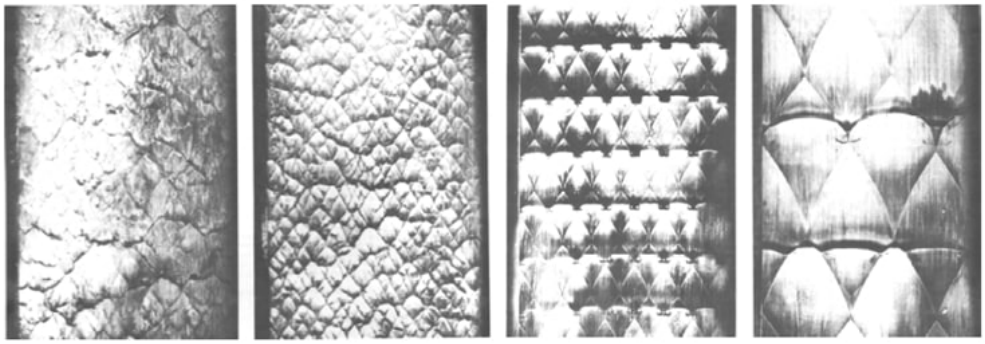

Figure 1.4: Experimental smoked foil records for different types of a combustible mixture (Voitsekhovskii et al., 1958)

In recent years, important progress has been made in achieving a direct correlation between dynamic parameters and this characteristic length scale. The degree of instability within the unsteady detonation structure is typically characterized by the associated cell irregularities observed from the smoked foils. Recent progress also proposed that the instabilities embedded within the detonation structure and the degree of cellular irregularities are intimately related to detonation dynamics and have a direct influence on its propagation, initiation, and failure (Lee, 1996; Radulescu and Lee, 2002; Radulescu et al., 2005; Ng and Zhang, 2012; Zhang, Liu, and Yan, 2019; Xiao and Radulescu, 2020; Yuan et al., 2021, etc.).

1.3 Limits and near-limit behavior of detonation

The detonation limits are defined as the critical conditions outside of which a detonation propagation cannot be self-sustained (Lee, 2008). In general, detonation limits can be brought about by changing the mixtures and initial condition, by too lean or too rich a mixture composition and an increase in the concentration of inert diluent, or by the decrease in initial pressure for a mixture of

a given composition. Alternatively, detonation limits could also be reached and investigated by the change of boundary conditions in a given geometry. In this thesis, 'limit' is defined as the condition where the influence of boundary conditions leads to the onset of detonation limit and below which a detonation fails to propagate.

When a detonation propagates in a relatively large tube where the wall boundary conditions do not affect significantly the core detonation structure, its propagation velocity is well predicted by the CJ theory. However, when a detonation is propagating in small tubes, due to losses and boundary effects, its velocity is smaller than the CJ value. This propagation regime is usually referred to as quasi-detonation (Teodorczyk, Lee, & Knystautas, 1989). The velocity deficit becomes more prominent as the limits are approached. Substantial studies have been performed in recent years investigating the steady velocity deficits of different mixtures in small tubes and channels near the limits (Kitano et al., 2009; Camargo et al., 2010; Ishii and Monwar, 2011; Gao et al., 2014; Wang et al., 2017; Cao et al., 2019; Zhang et al., 2020). The limits are usually defined by the sudden increase of the velocity deficit indicating a complete failure of the detonation propagation.

By observing the near-limit cellular detonation pattern, the unstable cellular structure is driven to lower unstable modes toward the limits, i.e., from multi-headed to single-head spinning detonation around the circumference of the tube (πd). The detonation limit also leads to the enlargement of the cell size (or transverse wave spacing) and the velocity fluctuations become increasingly large resulting in a detonation cellular front with strong irregularities and instabilities (Lee et al., 2013; Gao et al., 2014; Jackson et al., 2016; Zhang, 2016; Zhang, Liu, and Li, 2019).

Since single-headed spinning detonation corresponds to the limiting structure of a self-sustained detonation, any absence of cellular features at the detonation front could provide a better indication of the detonation failure. From a simple scale analysis, the limit can thus be defined as $\lambda = \pi d$, or the limit is defined as $d/\lambda = 1/3$.

1.4 Near-limit gaseous detonations in roughed-wall tubes

To further the understanding of boundary conditions on the near-limit propagation of detonation and subsequently its failure, many recent studies focus on the effect of wall roughness which could

also affect strongly both the propagation velocity and the structure of the detonation wave. To mimic wall roughness, numerous investigations have been carried out in the past few decades on detonation propagation in obstacle-filled tubes, where circular orifice plates with a large blockage ratio (BR), of the order of the diameter of the tube itself, are placed periodically at about one tube diameter apart along the length of the tube (Cross and Ciccarelli, 2015; Ciccarelli and Cross, 2016; Ciccarelli et al., 2017; Wang et al., 2017; Wang et al., 2018; Wang et al., 2019; Kellenberger and Ciccarelli, 2020; Sun and Lu, 2020, etc.).

In obstacle-filled tubes, the detonation velocity can be as low as half the Chapman-Jouguet (CJ) value. Photographic observations also indicate that the detonation structure can be significantly perturbed. However, the introduction of these large orifice plates completely changes the detonation dynamics and its propagation mechanism. In these settings, photographic observations indicate that the detonation frontal structure is often completely destroyed and the near-limit detonation propagation is hence governed by other additional mechanisms that include continuous diffraction, turbulent flame jetting, and re-initiation via diffracted shock reflection. Thus, it is difficult to consider these orifice plate-filled tubes as rough-walled tubes. For sufficiently large BRs, the propagation could approach a scene that resembled a series of DDTs where a decoupled front and large unburned pockets in an extended reaction zone are formed (Teodorczyk et al., 1990; Ciccarelli and Dorofeev, 2008;).

It is appropriate to define rough-walled tubes as those whose dimension of the wall roughness is small as compared to the tube diameter. In this way, the effect of the wall roughness creates only small perturbations on the detonation and the flow field associated with the detonation front. Detonation propagation in rough tubes was first investigated by Laffitte (1923) who used a strip of coarse sandpaper wrapped around the tube wall to create wall roughness. Alternatively, Shchelkin (1947) and Guénoche (1949), Brochet (1966), Teodorczyk and Teodorczyk and Lee (1995), Starr, Lee, and Ng (2015) and Zhang (2016) Zhang, Liu, and Wang (2017) used instead a spiral coiled wire inserted into the tube to generate wall roughness. These experiments were recently revisited by Ren et al.(2020, 2021); Liu et al. (2021) and a wealth of information on detonation velocity and smoked foils was obtained. Few of these studies suggest that wall roughness also tends to change a multi-headed detonation to a lower unstable mode (e.g., spinning detonation) and eventually fails due to

the absence of any cellular detonation structure. Due to the experimental limitations, relatively little detailed information on the effects of wall roughness and the resulting flow perturbation on the cellular quasi-detonation structures and their regularities is available. Intuitively, the wall roughness can have a competing effect on the detonation propagation. On one hand, the wall roughness can either generate flow fluctuation or is beneficial for unstable cellular detonation propagation, promoting auto-ignition in the reactive flow field. On the other hand, losses in momentum or boundary layer effects due to wall roughness in tubes can promote detonation failure. Hence, there is a need to observe how the detonation propagates in rough-walled tubes and how the detonation structure responds to the disturbances generated by the wall roughness.

1.5 Objective of the thesis

The objective of this study is to isolate the effect of flow perturbation caused by the confined boundary, particularly wall roughness, on the propagation of quasi-detonations and their cellular dynamics. To this end, this work conducts a simplified numerical simulation study modeling detonation propagating in rough tubes with a relatively small degree of roughness. To simplify the computational modeling effort while revealing some salient unstable characteristics of quasi-detonations propagating in rough tubes, the strategy adopted in this study is to conduct numerical simulations using an ideal-gas, reactive flow model given by the inviscid Euler equations with a simplified two-step chemical kinetic model (Ng et al., 2005). The roughness required for the formation of a quasi-detonation is simulated numerically by introducing small obstacles at the computational wall boundary, creating both velocity deficit and flow instability on the detonation front structure. This thesis reports a series of simulations to look at in a parametric manner how different degrees of wall roughness (by varying the obstacle heights), the physical confinement (by changing channel widths), and the chemical kinetics of the combustible mixtures influence the strength and cellular characteristics of quasi-detonation.

1.6 Thesis outline

The current Chapter 1 presents the research problem as well as some basic concepts and background information from the relevant literature. Chapter 2 describes in detail the physical models and numerical methods used in this numerical study. Chapter 3 presents the results of the numerical simulation and analysis of the effect of roughness on the detonation propagation. Chapter 4 describes some differences between staggered and aligned tubes. Finally, Chapter 5 summarizes the survey and provides suggestions for future work.

1.7 Contribution to knowledge

This investigation contributes, using numerical simulations, to the understanding of the effect of wall roughness on the cellular dynamics and near-limit behavior of quasi-detonation propagation. The parametric study identifies quantitatively key parameters which could play a prominent role in affecting the detonation instabilities, velocity deficit, and the limit phenomenon. This thesis includes published works in the following conference:

- **Lyu Y**, Yan C and Ng HD (2022) Numerical investigation of gaseous cellular detonation propagation in rough-walled channels. Proceeding of the Canadian Section of the Combustion Institute Spring Technical Meeting, University of Ottawa, Ottawa, ON, Canada, May 16-19, 2022.

- **Lyu Y**, Yan C and Ng HD (2023) Effects of wall roughness on the cellular pattern evolution and failure of gaseous detonations. Accepted for the 17th Asian Congress of Fluid Mechanics (ACFM), Beijing, China, Aug. 8-12, 2023.

Chapter 2

Formulations and Methods

This work employs computational approaches based on earlier research on cellular detonation simulations. In this Chapter, the physical model for an ideal gas, reactive flow, and the validation of the computational approach is presented. Here, the second-order MUSCL-Hancock scheme and an HLLC (Harten-Lax-van Leer-contact) approximation Riemann solver are used to solve numerically the governing equations. To achieve higher computational performance and acceleration, the numerical solver is built utilizing the NVIDIA CUDA framework and runs on Graphical Processing Unit (GPU) hardware.

2.1 Governing equations

Recent advances in numerical techniques and computer technology have enabled the accurate integration of the nonlinear reactive Euler equations with sufficient spatial and temporal resolutions to resolve the fine-scale features in the detonation reaction zone. In contrast to linear stability analysis, the unstable flow phenomenon may be more readily investigated utilizing direct numerical simulation, which keeps the complete nonlinear behavior. In addition, unlike experiments, numerical simulations have the benefit of being easily controllable in terms of the number of spatial dimensions. As a result, we may analyze one-dimensional, longitudinal instabilities in isolation before moving on to more complex instabilities in higher dimensions. This allows for a more accurate interpretation of the numerical data obtained. In a practical experiment, it is difficult to suppress the

instability in other dimension(s) to simplify the interpretation of the results. Numerical analyses can also reveal more information about the overall flow field that is difficult, if not unattainable, to measure experimentally. To simplify the computational modeling effort while revealing some salient unstable characteristics of quasi-detonations propagating in rough tubes, the strategy adopted in this study is to conduct numerical simulations using an ideal-gas, reactive flow model given by the inviscid Euler equations. In this ideal model, the viscous effect is ignored due to the high Reynolds number flow dominated by convective inertia. The diffusion effect is also neglected due to its longer time scale relative to the convective phenomenon.

To mimic the chemical reaction of the combustible mixture, a two-step induction-reaction model is used. The governing equations are solved numerically using a second-order finite-volume method enabled by parallel Graphics Processing Unit (GPU) computing. Hence, the ideal gas, reactive flow model given by the inviscid Euler equations with two-step induction-reaction kinetics is represented as follows:

$$\frac{\partial \mathbf{U}}{\partial t} + \frac{\partial \mathbf{F}}{\partial x} + \frac{\partial \mathbf{G}}{\partial y} = \mathbf{S} \tag{1}$$

$$\mathbf{U} = \begin{bmatrix} \rho \\ \rho u \\ \rho v \\ \rho e \\ \rho \xi \\ \rho \beta \end{bmatrix}, \quad \mathbf{F} = \begin{bmatrix} \rho u \\ \rho u^2 + p \\ \rho uv \\ (\rho e + p)\, u \\ \rho u \xi \\ \rho u \beta \end{bmatrix}, \quad \mathbf{G} = \begin{bmatrix} \rho v \\ \rho uv \\ \rho v^2 + p \\ (\rho e + p)\, v \\ \rho v \xi \\ \rho v \beta \end{bmatrix}, \quad \mathbf{S} = \begin{bmatrix} 0 \\ 0 \\ 0 \\ 0 \\ \dot{\omega}_{\mathrm{I}} \\ \dot{\omega}_{\mathrm{R}} \end{bmatrix} \tag{2}$$

where variables ρ, u, v, p, ξ, β, e, and Q denotes the density, velocities in x- and y- direction, pressure, induction progress, product fraction, energy, and the amount of total chemical heat release, respectively. $\mathbf{U}$ is the conserved variable, $\mathbf{F}$ and $\mathbf{G}$ are the convective fluxes, and $\mathbf{S}$ is the reactive source term, then for the polytropic equation of state e is the total energy per unit mass.

$$e = \frac{p}{(\gamma - 1)\rho} + \frac{u^2 + v^2}{2} - \beta Q \tag{3}$$

and for the ideal gas:

$$p = \rho T \tag{4}$$

where the first term in equation (3) is the specific internal energy, the second term is the kinetic energy, and the third term is the heat release. All the terms, parameters, and variables have been non-dimensionalized by reference to the quiescent unburned state ahead of the detonation front (Ng et al., 2005).

$$\rho = \frac{\widetilde{\rho}}{\rho_0},\ p = \frac{\widetilde{p}}{p_0},\ T = \frac{\widetilde{T}}{T_0},\ u = \frac{\widetilde{u}}{\sqrt{RT_0}},\ x = \frac{\widetilde{x}}{x_{ref}},\ Q = \frac{\widetilde{Q}}{RT_0},\ E_{\mathrm{a}} = \frac{\widetilde{E_{\mathrm{a}}}}{RT_0} \tag{5}$$

Again, a two-step induction-reaction Arrhenius kinetic model has been used to describe the source terms $\mathbf{S}$ which includes an induction zone with an additional advection equation for ξ. Compared with the one-step model, a two-step kinetic model has its advantages where the heat-releasing reactions at the end of the induction period are replaced by a suitably calibrated chemical transformation process (Ng et al., 2005).

$$\dot{\omega}_{\mathrm{I}} = H\left(1-\xi\right) k_{\mathrm{I}} \rho exp\left[E_{\mathrm{I}}\left(\frac{1}{T_s} - \frac{1}{T}\right)\right] \tag{6}$$

$$\dot{\omega}_{\mathrm{R}} = \left[1 - H\left(1-\xi\right)\right]\left(1-\beta\right) k_{\mathrm{R}} \rho exp\left(\frac{-E_{\mathrm{R}}}{T}\right) \tag{7}$$

where $\dot{\omega}_{\mathrm{I}}$ and $\dot{\omega}_{\mathrm{R}}$ are the induction and reaction rate, respectively. The reaction sensitivity is governed by E_{I} and E_{R}. E_{I} is the activation energy of the thermally neutral induction process, and E_{R} is the activation energy of the exothermic reaction.

The Heaviside step function $H(1-\xi)$ is given by:

$$H\left(1-\xi\right) = \begin{cases} 1, & \xi \leq 1 \\ 0, & \xi > 1 \end{cases} \tag{8}$$

ξ is introduced as a reaction progress variable for the induction process. When $\xi \leq 1$, $H(1-\xi) = 1$, represents the detonation shock spread in the induction zone, till $\xi = 1$ reaches the end of the

induction zone; when $\xi > 1$, $H(1-\xi) = 0$, the detonation shock come to the reaction zone which is similar to that of the one-step method, describe energy release in this zone.

In the two-step model, the unit length also called the reference length scale x_{ref} is chosen such that the one-dimensional ZND induction length is a unit. That is to say, the pre-exponential factor k_{I} of the induction step is used to define the reference length scale so that the induction length is unit, i.e., $\Delta_{\mathrm{I}} = 1$, or $k_{\mathrm{I}} = -u_{vn}$ (Ng et al., 2005), where the von Neumann speed u_{vn} is the particle velocity behind the shock front in the shock-fixed frame for the Chapman-Jouguet (CJ) detonation:

$$u_{vn} = \sqrt{\gamma}\frac{2 + (\gamma - 1)\,{M_{\mathrm{CJ}}}^2}{(\gamma + 1)\,M_{\mathrm{CJ}}} \tag{9}$$

Also from the Rankine-Hugoniot relationships (Ng & Zhang, 2012), the Mach number of Chapman-Jouguet detonation can be stood for corresponding a given Q:

$$M_{\mathrm{CJ}} = \frac{D}{c_0} = \sqrt{\left(1 + \frac{\gamma^2 - 1}{\gamma}Q\right) + \sqrt{\left(1 + \frac{\gamma^2 - 1}{\gamma}Q\right)^2 - 1}} \tag{10}$$

Also in formulas (6) and (7), β is the reaction process variable; k_{R} is the pre-exponential factor to vary the reaction zone structure (Ng et al., 2005).

Like the non-dimensionalization in previous studies, the energy release Q and two associated activation energies E_{I} and E_{R} have been scaled with RT_0. For convenience, an alternative scaling T_s is used for replacing the activation energies:

$$E_{\mathrm{I}} = T_s\varepsilon_{\mathrm{I}} \qquad E_{\mathrm{R}} = T_s\varepsilon_{\mathrm{R}} \tag{11}$$

where T_s is the post-shock temperature jumping across the leading front shock:

$$T_s = \frac{\left[2\gamma{M_{\mathrm{CJ}}}^2 - (\gamma - 1)\right]\left[2 + (\gamma - 1)\,{M_{\mathrm{CJ}}}^2\right]}{(\gamma + 1)^2\,{M_{\mathrm{CJ}}}^2} \tag{12}$$

When it comes to typical hydrocarbon mixtures, the reduced activation energy of the induction stage ε_{I} is large, because a high energy level in the induction zone is required to break the strong chemical bonds of the fuel and transfer it into radicals. Typical values for ε_{I} usually range from 4 (for H_2-O_2 mixture) to 12 (for heavy hydrocarbon mixtures).

On the contrary, the second step involves only reactions between energetic free radicals. For typical chain-branching reactions, therefore, the first step in the induction process generally is larger activation energy compared to the second step. As a result of that, for the present study, we have:

$$E_{\mathrm{I}} \gg E_{\mathrm{R}} \quad \varepsilon_{\mathrm{I}} \gg \varepsilon_{\mathrm{R}} \tag{13}$$

In this study, the same dimensionless thermodynamic parameters of the combustible mixture as in Yan, Ng, and Mi (2022) Yuan et al. (2021) are considered, i.e., Q = 21.365, γ = 1.32, T_s = 5.0373, E_{I} = 5.414T_s, E_{R} = 1.0T_s, k_{I} = 1.0022, k_{R} = 1.0, 2.0 or 4.0 and the Chapman–Jouguet (CJ) detonation velocity V_{CJ} = 5.858. These thermodynamic properties approximately represent the Zel'dovich-von Neumann-Doring (ZND) detonation structure of the stoichiometric hydrogen-oxygen mixture at 20 kPa and 300 K, giving rise to an unstable CJ detonation wave with a relatively irregular cellular pattern.

2.2 Numerical methods

2.2.1 Operator splitting

For a two-dimensional simulation, the governing equations for the chemically reactive flow can be represented as:

$$\frac{\partial \mathbf{U}}{\partial t} + \frac{\partial \mathbf{F}\left(\mathbf{U}\right)}{\partial x} + \frac{\partial \mathbf{G}\left(\mathbf{U}\right)}{\partial y} = \mathbf{S}\left(\mathbf{U}\right) \tag{14}$$

$\mathbf{F}$ and $\mathbf{G}$ are the convection fluxes of x- and y- direction, respectively, and $\mathbf{S}$ is the reaction source term to model the chemical energy released from the reaction. If the entire operators are being solved at the same time in a single time-step Δt, the process will be technically involved using un-splitter numerical techniques (Ng et al., 2005).

The method of fractional steps is formulated for the numerical integration to treat separately the hydrodynamics process and the chemical reaction process.

Denoting L_{C} and L_{S} to be the operators for the convective terms in each direction and the source term, respectively, the operating scheme thus follows:

$$\frac{\partial \mathbf{U}}{\partial t} = -L_{\mathrm{C_X}}\mathbf{U} \qquad \frac{\partial \mathbf{U}}{\partial t} = -L_{\mathrm{C_Y}}\mathbf{U} \qquad \frac{\partial \mathbf{U}}{\partial t} = \mathbf{S}\left(\mathbf{U}\right) \tag{15}$$

To obtain a second-order splitting scheme as follows:

$$\mathbf{U}_i^{n+1} = \mathbf{U}_i^n \cdot L_{\mathrm{C_X}}^{\Delta t/2} \cdot L_{\mathrm{C_Y}}^{\Delta t/2} \cdot L_{\mathrm{S}}^{\Delta t} \cdot L_{\mathrm{C_Y}}^{\Delta t/2} \cdot L_{\mathrm{C_X}}^{\Delta t/2} \tag{16}$$

2.2.2 Riemann problem and Godunov's method

Several effective high-resolution numerical techniques for systems of hyperbolic partial differential equations have been developed in recent years. Many of today's high-resolution numerical schemes are based on upwind differencing and are best suited for numerically solving systems of hyperbolic conservation laws because they introduce characteristic information about the local directionality of flow along the interface of spatially discontinuous cells. To assess the flow term at the cell interface, these upwind differential methods sometimes involve solving the associated local Riemann problem, which substantially complicates the upwind procedure (Toro, 2013).

The numerical method used here to approximate the solution of the hyperbolic conservation law employs the unit volume approach, where the integral formulation of the conservation law is directly discretized in physical space.

Consider the general Initial-Boundary Value Problem (IBVP) for non-linear systems of hyperbolic conservation laws:

Partial differential equations(PDEs):

$$\mathbf{U}_t + \mathbf{F}\left(\mathbf{U}\right)_x = 0 \tag{17}$$

Initial conditions(ICs):

$$\mathbf{U}\left(x, 0\right) = \mathbf{U}^{(0)}\left(x\right) \tag{18}$$

Boundary conditions(BCs):

$$\mathbf{U}(0, t) = \mathbf{U}_l(t), \quad \mathbf{U}\left(L, t\right) = \mathbf{U}_r\left(t\right) \tag{19}$$

Where $\mathbf{U}$ is the conserved variables and $\mathbf{F}(\mathbf{U})$ is the convective fluxes. The initial conditions are illustrated in Fig. 2.1. $\mathbf{U}_i^{n+1}$ and $\mathbf{U}_i^n$ are the conserved variables at the next and current time levels, $n+1$ and n, respectively. $\mathbf{F}_{i-\frac{1}{2}}$ and $\mathbf{F}_{i+\frac{1}{2}}$ are the numerical fluxes at the interfaces of the computational cells of the discretized space. (Ng et al., 2005) The updated finite volume formula was obtained by considering the equivalent integral formula:

$$\oint [\mathbf{U}dx + \mathbf{F}(\mathbf{U})dt] = 0 \tag{20}$$

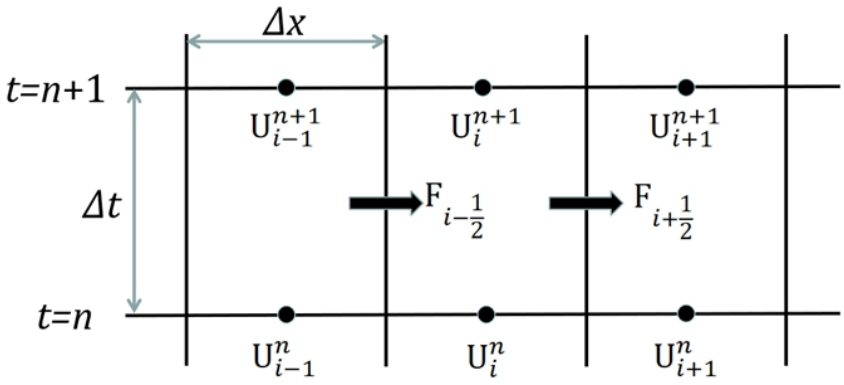

Figure 2.1: Geometrical illustration of the finite volume update formula.

For a 1-D system, the Godunov method can be written in a conservative form:

$$\mathbf{U}_i^{n+1} = \mathbf{U}_i^n + \frac{\Delta t}{\Delta x}[\mathbf{F}_{i-\frac{1}{2}} - \mathbf{F}_{i+\frac{1}{2}}] \tag{21}$$

With inter-cell numerical flux given by

$$\mathbf{F}_{i+\frac{1}{2}} = \mathbf{F}\left(\mathbf{U}_{i+\frac{1}{2}}(0)\right) \tag{22}$$

Also, the time step should satisfy:

$$\Delta t \leq \frac{\Delta x}{\mathbf{S}_{\max}^n} \tag{23}$$

where $\mathbf{U}_{i+\frac{1}{2}}(0)$ is the exact similarity solution $\mathbf{U}_{i+\frac{1}{2}}(x/t)$ to the Riemann problem, computed at $x/t = 0$. The structure of the Riemann problem consists of left and right shock waves or rarefaction waves in various allowed combinations, separated by a contact surface.

Here we set x_{L} and x_{R} in the control volume $[x_{\mathrm{L}}, x_{\mathrm{R}}] \times [0, T]$, $x_{\mathrm{L}} \leq T\mathbf{S}_{\mathrm{L}}, x_{\mathrm{R}} \geq T\mathbf{S}_{\mathrm{R}}$ where $\mathbf{S}_{\mathrm{L}}$ and $\mathbf{S}_{\mathrm{R}}$ are the fastest signal velocities perturbing the initial data states $\mathbf{U}_{\mathrm{L}}$ and $\mathbf{U}_{\mathrm{R}}$ respectively, and T is a chosen time. From

$$\mathbf{U}_t + \mathbf{F}(\mathbf{U})_x = 0$$

$$\mathbf{U}(x,0) = \begin{cases} \mathbf{U}_{\mathrm{L}} & \text{if } x < 0 \\ \mathbf{U}_{\mathrm{R}} & \text{if } x > 0 \end{cases} \tag{24}$$

In the control volume $[x_{\mathrm{L}}, x_{\mathrm{R}}] \times [0, T]$ we would have:

$$\int_{x_{\mathrm{L}}}^{x_{\mathrm{R}}} \mathbf{U}(x,T)dx = \int_{x_{\mathrm{L}}}^{x_{\mathrm{R}}} \mathbf{U}(x,0)dx + \int_0^T \mathbf{F}\left(\mathbf{U}\left(x_{\mathrm{L}},t\right)\right)dt - \int_0^T \mathbf{F}\left(\mathbf{U}\left(x_{\mathrm{R}},t\right)\right)dt \tag{25}$$

Based on integral forms of conservation law, we can reach:

$$\int_{T\mathbf{S}_{\mathrm{L}}}^{T\mathbf{S}_{\mathrm{R}}} \mathbf{U}(x,T)dx = T\left(\mathbf{S}_{\mathrm{R}}\mathbf{U}_{\mathrm{R}} - \mathbf{S}_{\mathrm{L}}\mathbf{U}_{\mathrm{L}} + \mathbf{F}_{\mathrm{L}} - \mathbf{F}_{\mathrm{R}}\right) \tag{26}$$

Where $\mathbf{F}_{\mathrm{L}} = \mathbf{F}\left(\mathbf{U}_{\mathrm{L}}\right)$ and $\mathbf{F}_{\mathrm{R}} = \mathbf{F}\left(\mathbf{U}_{\mathrm{R}}\right)$

On division through by the length $T(\mathbf{S}_{\mathrm{R}} - \mathbf{S}_{\mathrm{L}})$ which is the width of the wave system of the solution of the Riemann problem between the slowest and fastest signals at a chosen time T.

$$\frac{1}{T\left(\mathbf{S}_{\mathrm{R}} - \mathbf{S}_{\mathrm{L}}\right)} \int_{T\mathbf{S}_{\mathrm{L}}}^{T\mathbf{S}_{\mathrm{R}}} \mathbf{U}(x,T)dx = \frac{\mathbf{S}_{\mathrm{R}}\mathbf{U}_{\mathrm{R}} - \mathbf{S}_{\mathrm{L}}\mathbf{U}_{\mathrm{L}} + \mathbf{F}_{\mathrm{L}} - \mathbf{F}_{\mathrm{R}}}{\mathbf{S}_{\mathrm{R}} - \mathbf{S}_{\mathrm{L}}} \tag{27}$$

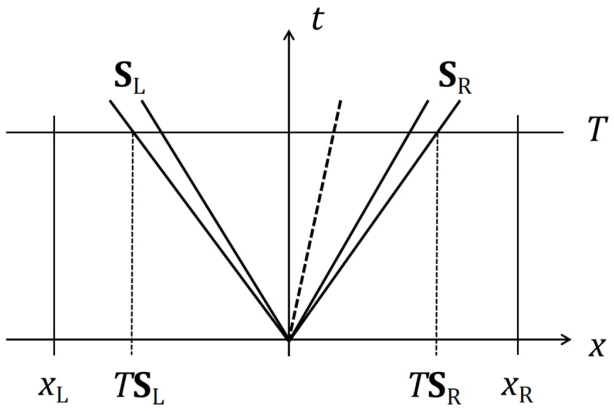

Figure 2.2: Control volume $[x_{\mathrm{L}}, x_{\mathrm{R}}] \times [0, T]$ on x-t plane. $\mathbf{S}_{\mathrm{L}}$ and $\mathbf{S}_{\mathrm{R}}$ are the fastest signal velocities arising from the solution of the Riemann problem.

2.2.3 HLLC approximate Riemann solver

To directly compute numerical fluxes, approximation techniques have been developed to approximately solve the Riemann problem, and the resulting algorithms are known as Harten, Lax, and van Leer (HLL) approximate Riemann solvers. Unlike analytical methods for solving exact Riemann problems, which are informative and time-consuming, approximate Riemann solvers directly give estimates of numerical fluxes between cells, and the difference in results is usually negligible. The HLL Riemann solver assumes a single constant state between two nonlinear waves (shock or rarefaction) and requires estimates for the fastest signal velocities emerging from the initial discontinuity at the interface, resulting in a two-wave model for the solution structure of the problem. The HLLC scheme used in this work is an extension of the HLL scheme in which the missing contact and shear waves are put back into the structure of the original approximate solver. The HLLC scheme provides a more accurate approach through a three-wave model, preserving the solution structure with shock, contact, and shear waves. To compute wave speeds of the left-going and right-going waves $\mathbf{S}_{\mathrm{L}}$ and $\mathbf{S}_{\mathrm{R}}$, the pressure-velocity-based wave estimation proposed by (Toro, 2013) is used to accurately estimate shock and rarefaction waves.

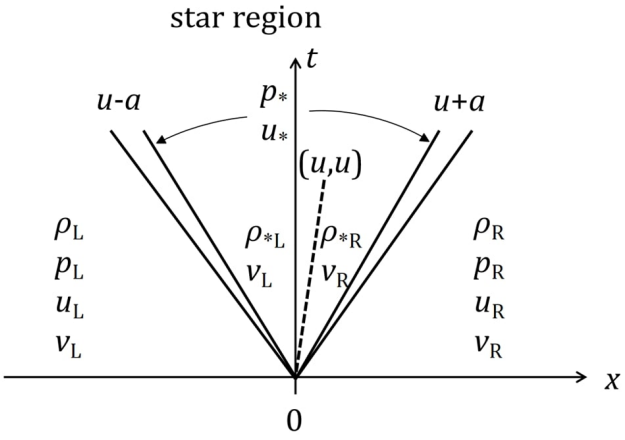

Figure 2.3: Waves structure of the exact solution $\mathbf{U}_{i+\frac{1}{2}}(x/t)$ of the Riemann Problem for the one-dimensional Euler equations.

From the Figure. 2.3 and 2.4 , we can get:

$$\frac{1}{T\left(\mathbf{S}_{\mathrm{R}}-\mathbf{S}_{\mathrm{L}}\right)}\int_{T\mathbf{S}_{\mathrm{L}}}^{T\mathbf{S}_{\mathrm{R}}}\mathbf{U}(x,T)dx=\frac{1}{T\left(\mathbf{S}_{\mathrm{R}}-\mathbf{S}_{\mathrm{L}}\right)}\int_{T\mathbf{S}_{\mathrm{L}}}^{T\mathbf{S}_{*}}\mathbf{U}(x,T)dx+\frac{1}{T\left(\mathbf{S}_{\mathrm{R}}-\mathbf{S}_{\mathrm{L}}\right)}\int_{T\mathbf{S}_{*}}^{T\mathbf{S}_{\mathrm{R}}}\mathbf{U}(x,T)dx \tag{28}$$

In the control volume $[x_{\mathrm{L}},x_{\mathrm{R}}]\times[0,T]$ we would have:

$$\begin{aligned}\mathbf{U}_{*\mathrm{L}}&=\frac{1}{T\left(\mathbf{S}_{*}-\mathbf{S}_{\mathrm{L}}\right)}\int_{T\mathbf{S}_{\mathrm{L}}}^{T\mathbf{S}_{*}}\mathbf{U}(x,T)dx\\ \mathbf{U}_{*\mathrm{R}}&=\frac{1}{T\left(\mathbf{S}_{\mathrm{R}}-\mathbf{S}_{*}\right)}\int_{T\mathbf{S}_{*}}^{T\mathbf{S}_{\mathrm{R}}}\mathbf{U}(x,T)dx\end{aligned} \tag{29}$$

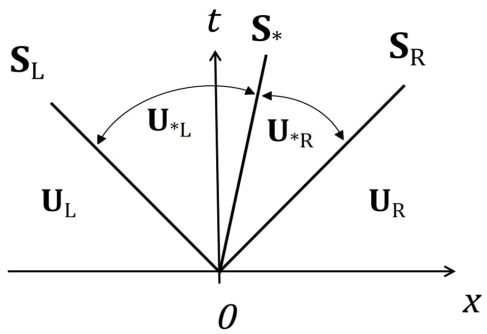

Figure 2.4: HLLC approximate Riemann solver. The solution in the star region consists of two constant states separated from each other by a middle wave of speed $\mathbf{S}_*$.

The HLLC approximate Riemann solver is given as follows:

$$\widetilde{\mathbf{U}}(x,t) = \begin{cases} \mathbf{U}_{\mathrm{L}}, & \text{if } \frac{x}{t} \leq \mathbf{S}_{\mathrm{L}} \\ \mathbf{U}_{*\mathrm{L}}, & \text{if } \mathbf{S}_{\mathrm{L}} \leq \frac{x}{t} \leq \mathbf{S}_{*} \\ \mathbf{U}_{*\mathrm{R}}, & \text{if } \mathbf{S}_{*} \leq \frac{x}{t} \leq \mathbf{S}_{\mathrm{R}} \\ \mathbf{U}_{\mathrm{R}}, & \text{if } \frac{x}{t} \geq \mathbf{S}_{\mathrm{R}} \end{cases} \tag{30}$$

And for the flux:

$$\mathbf{F}_{i+\frac{1}{2}}^{\mathrm{HLLC}} = \begin{cases} \mathbf{F}_{\mathrm{L}}, & \text{if } 0 \leq \mathbf{S}_{\mathrm{L}}, \\ \mathbf{F}_{*\mathrm{L}}, & \text{if } \mathbf{S}_{\mathrm{L}} \leq 0 \leq \mathbf{S}_{*}, \\ \mathbf{F}_{*\mathrm{R}}, & \text{if } \mathbf{S}_{*} \leq 0 \leq \mathbf{S}_{\mathrm{R}}, \\ \mathbf{F}_{\mathrm{R}}, & \text{if } 0 \geq \mathbf{S}_{\mathrm{R}}. \end{cases} \tag{31}$$

Where $\mathbf{F}_{*\mathrm{L}}$ and $\mathbf{F}_{*\mathrm{R}}$ still need to be determined. Then for the HLLC flux in the Euler equations, we need to find the solution for the two unknown intermediate fluxes $\mathbf{F}_{*\mathrm{L}}$ and $\mathbf{F}_{*\mathrm{R}}$. By applying Rankine-Huguenot conditions across each of the waves of speeds $\mathbf{S}_{\mathrm{L}}$, $\mathbf{S}_{*}$, and $\mathbf{S}_{\mathrm{R}}$, we obtain:

$$\begin{aligned} \mathbf{F}_{*\mathrm{L}} &= \mathbf{F}_{\mathrm{L}} + \mathbf{S}_{\mathrm{L}} \left(\mathbf{U}_{*\mathrm{L}} - \mathbf{U}_{\mathrm{L}} \right) \\ \mathbf{F}_{*\mathrm{R}} &= \mathbf{F}_{*\mathrm{L}} + \mathbf{S}_{*} \left(\mathbf{U}_{*\mathrm{R}} - \mathbf{U}_{*\mathrm{L}} \right) \\ \mathbf{F}_{*\mathrm{R}} &= \mathbf{F}_{\mathrm{R}} + \mathbf{S}_{\mathrm{R}} \left(\mathbf{U}_{*\mathrm{R}} - \mathbf{U}_{\mathrm{R}} \right) \end{aligned} \tag{32}$$

Then we have 3 equations and 4 unknowns($\mathbf{F}_{*\mathrm{L}}$, $\mathbf{F}_{*\mathrm{R}}$, $\mathbf{U}_{*\mathrm{L}}$ and $\mathbf{U}_{*\mathrm{R}}$). We have exact solutions for pressure, the normal component of velocity:

$$\begin{aligned} p_{*\mathrm{L}} &= p_{*\mathrm{R}} = p_{*} \\ u_{*\mathrm{L}} &= u_{*\mathrm{R}} = u_{*} \end{aligned} \tag{33}$$

And then for tangential velocity components, we have:

$$\begin{aligned} v_{*\mathrm{L}} &= v_{\mathrm{L}}, v_{*\mathrm{R}} = v_{\mathrm{R}} \\ w_{*\mathrm{L}} &= w_{\mathrm{L}}, w_{*\mathrm{R}} = w_{\mathrm{R}} \end{aligned} \tag{34}$$

Based on the Riemann Problem for the Euler Equations, for convenience, we make the wave of

speeds as:

$$\mathbf{S}_* = u_* \tag{35}$$

And thus we can estimate the value of $\mathbf{S}_*$, then the normal velocity component in the star region u_* is also known. After which, we have:

$$\begin{aligned} \mathbf{S}_\mathrm{L}\mathbf{U}_{*\mathrm{L}} - \mathbf{F}_{*\mathrm{L}} &= \mathbf{S}_\mathrm{L}\mathbf{U}_\mathrm{L} - \mathbf{F}_\mathrm{L} \\ \mathbf{S}_\mathrm{R}\mathbf{U}_{*\mathrm{R}} - \mathbf{F}_{*\mathrm{R}} &= \mathbf{S}_\mathrm{R}\mathbf{U}_\mathrm{R} - \mathbf{F}_\mathrm{R} \end{aligned} \tag{36}$$

Where the right-hand sides of both equations are known as constant vectors.

We can assume $\mathbf{S}_\mathrm{L}$ and $\mathbf{S}_\mathrm{R}$ are known, do the algebraic calculation, we would have two equations about pressures:

$$\begin{aligned} p_{*\mathrm{L}} &= p_\mathrm{L} + \rho_\mathrm{L}\left(\mathbf{S}_\mathrm{L} - u_\mathrm{L}\right)\left(\mathbf{S}_* - u_\mathrm{L}\right) \\ p_{*\mathrm{R}} &= p_\mathrm{R} + \rho_\mathrm{R}\left(\mathbf{S}_\mathrm{R} - u_\mathrm{R}\right)\left(\mathbf{S}_* - u_\mathrm{R}\right) \end{aligned} \tag{37}$$

Where

$$\begin{aligned} \mathbf{F}_{*\mathrm{L}} &= u_\mathrm{L} \cdot \mathbf{U}_{*\mathrm{L}} + p_{*\mathrm{L}} \\ \mathbf{U}_{*\mathrm{L}} &= u_{*\mathrm{L}} \cdot \rho_{*\mathrm{L}} \\ \mathbf{F}_{*\mathrm{R}} &= u_\mathrm{R} \cdot \mathbf{U}_{*\mathrm{R}} + p_{*\mathrm{R}} \\ \mathbf{U}_{*\mathrm{R}} &= u_{*\mathrm{R}} \cdot \rho_{*\mathrm{R}} \end{aligned} \tag{38}$$

Because $p_{*\mathrm{L}} = p_{*\mathrm{R}}$, we can obtain the speed $\mathbf{S}_*$ by using $\mathbf{S}_\mathrm{L}$ and $\mathbf{S}_\mathrm{R}$:

$$\mathbf{S}_* = \frac{p_\mathrm{R} - p_\mathrm{L} + \rho_\mathrm{L} \cdot u_\mathrm{L}\left(\mathbf{S}_\mathrm{L} - u_\mathrm{L}\right) - \rho_\mathrm{R} \cdot u_\mathrm{R}\left(\mathbf{S}_\mathrm{R} - u_\mathrm{R}\right)}{\rho_\mathrm{L}\left(\mathbf{S}_\mathrm{L} - u_\mathrm{L}\right) - \rho_\mathrm{R}\left(\mathbf{S}_\mathrm{R} - u_\mathrm{R}\right)} \tag{39}$$

Thus, we only need to provide estimates for $\mathbf{S}_\mathrm{L}$ and $\mathbf{S}_\mathrm{R}$, just as for the simpler HLL solver. For $\mathrm{K} = \mathrm{L}$ and $\mathrm{K} = \mathrm{R}$, it is easy to find out that:

$$\mathbf{F}_{*\mathrm{K}} = \mathbf{F}_\mathrm{K} + \mathbf{S}_\mathrm{K}\left(\mathbf{U}_{*\mathrm{K}} - \mathbf{U}_\mathrm{K}\right) \tag{40}$$

Then we can get:

$$\mathbf{U}_{*\mathrm{K}} = \rho_{\mathrm{K}} \left(\frac{\mathbf{S}_{\mathrm{K}} - \mathbf{U}_{\mathrm{K}}}{\mathbf{S}_{\mathrm{K}} - \mathbf{S}_{*}} \right) \begin{bmatrix} 1 \\ \mathbf{S}_{*} \\ v_{\mathrm{K}} \\ w_{\mathrm{K}} \\ \frac{\mathbf{E}_{\mathrm{K}}}{\rho_{\mathrm{K}}} + (\mathbf{S}_{*} - \mathbf{U}_{\mathrm{K}}) \left[\mathbf{S}_{*} + \frac{p_{\mathrm{K}}}{\rho_{\mathrm{K}}(\mathbf{S}_{\mathrm{K}} - \mathbf{U}_{\mathrm{K}})} \right] \end{bmatrix} \tag{41}$$

Where

$$\mathbf{F}_{i+\frac{1}{2}}^{\mathrm{HLLC}} = \begin{cases} \mathbf{F}_{\mathrm{L}}, & \text{if } 0 \leq \mathbf{S}_{\mathrm{L}}, \\ \mathbf{F}_{*\mathrm{L}}, & \text{if } \mathbf{S}_{\mathrm{L}} \leq 0 \leq \mathbf{S}_{*}, \\ \mathbf{F}_{*\mathrm{R}}, & \text{if } \mathbf{S}_{*} \leq 0 \leq \mathbf{S}_{\mathrm{R}}, \\ \mathbf{F}_{\mathrm{R}}, & \text{if } 0 \geq \mathbf{S}_{\mathrm{R}}. \end{cases} \tag{42}$$

2.2.4 MUSCL-Hancock scheme

This method is different from the Godunov method which applies on first-order, MUSCL can achieve higher-order accuracy. Our research uses a second-order to improve accuracy. By reconstructing values across each cell boundary, data evolution through time steps, and solving the Riemannian problem, MUSCL-Hancock reconstruction allows better second-order accuracy than using piecewise constant values. The next section presents a total variation decreasing (TVD) version of MUSCL-Hancock.

The simplest way of modifying the piecewise constant data u_i^n is to replace the constant states u_i^n with piecewise linear functions $u_i(x)$. As for the first–order Godunov method, one assumes that u_i^n represents an integral average in cell $I_i = [x_{i-\frac{1}{2}}, x_{i+\frac{1}{2}}]$ as given by the below equation:

$$u_i^n = \frac{1}{\Delta x} \int_{x_{i-\frac{1}{2}}}^{x_{i+\frac{1}{2}}} u\left(x, t^n\right) dx. \tag{43}$$

In short, u_i^n represents an integral average in a cell $I_i = [x_{i-\frac{1}{2}}\ ,\ x_{i+\frac{1}{2}}]$ in first-order Godunov Method.

A piecewise linear, local reconstruction of u_i^n

$$u_i(x) = u_i^n + \frac{(x - x_i)}{\Delta x}\Delta_i, x \in [0, \Delta x] \tag{44}$$

where $\Delta_i/\Delta x$ is a suitably chosen slope of $u_i(x)$ in cell I_i, we can call Δ_i as slope in the following parts. Then, the solution $u_i(x)$ belongs to the exact cell I_i because its range of it is $x \in [0, \Delta x]$.

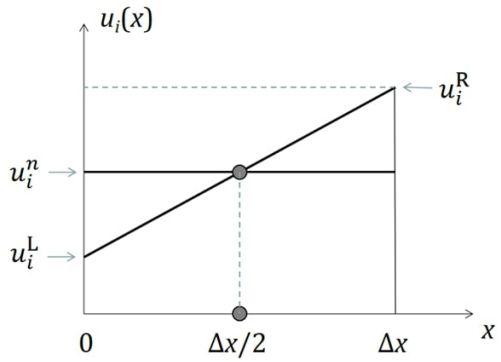

Figure 2.5: Piece-wise linear MUSCL reconstruction of data in a single computing cell I_i, boundary extrapolated values are u_i^{L}, u_i^{R}.

The centre of the cell x_i in local co-ordinates is $x = \frac{1}{2}\Delta x$ and $u_i\left(x_i\right) = u_i^n$, so on the boundary we have:

$$\begin{cases} u_i^{\mathrm{L}} = u_i(0) = u_i^n - \frac{1}{2}\Delta_i \\ u_i^{\mathrm{R}} = u_i(\Delta x) = u_i^n - \frac{1}{2}\Delta_i \end{cases} \tag{45}$$

Note that the integral of $u_i(x)$ in cell I_i is identical to that of u_i^n.

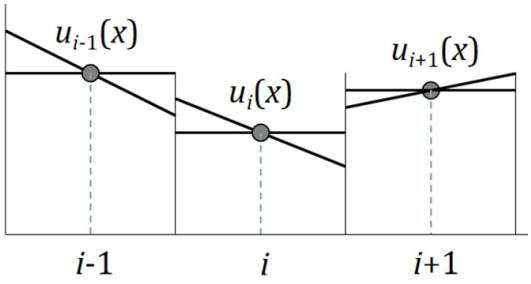

Figure 2.6: Piece-wise linear MUSCL reconstruction for three successive computing cells I_{i-1}, I_i, I_{i+1}.

Then we give more cells like in the graph above. Generalized Riemann Problem is denied here

to solve Flux $f_{i+\frac{1}{2}}$ in each cell at each interface $i+\frac{1}{2}$: (called Generalized Riemann problem)

$$\begin{cases} u_t + f(u)_x = 0, & \text{(PDEs)} \\ u(x,0) = \begin{cases} u_i(x), & x < 0 \\ u_{i+1}(x), & x > 0 \end{cases} \end{cases} \tag{46}$$

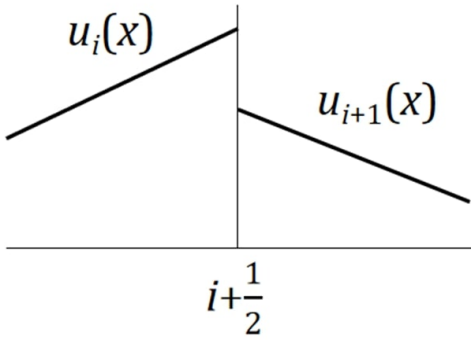

Figure 2.7: Piecewise linear data.

The solution no longer contains uniform regions as in the conventional Riemann problem in which the data is piecewise constant; wave paths are now curved in x-t space.

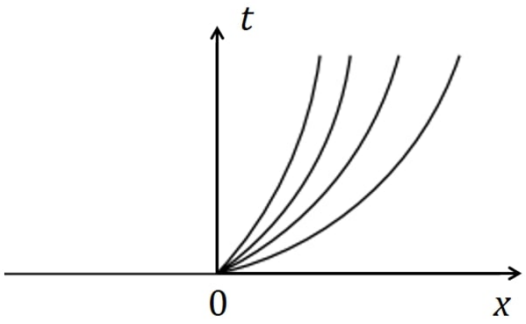

Figure 2.8: Structure of the solution in x–t plane.

In one easier way, we may give up the solution of the generalized Riemann problem and rely on the use of the boundary extrapolated values u_i^{L},u_i^{R} for each function $u_i(x)$. Then we consider the

piecewise constant data Riemann problem:

$$\begin{cases} u_t + f(u)_x = 0, & \text{(PDEs)} \\ u(x,0) = \begin{cases} u_i^{\mathrm{R}}, & x < 0 \\ u_{i+1}^{\mathrm{L}}, & x > 0 \end{cases} \end{cases} \tag{47}$$

Then, we define the slopes of Δ_i like:

$$\Delta_i = \frac{1}{2}(1+\omega)\cdot\Delta u_{i-\frac{1}{2}} + \frac{1}{2}(1-\omega)\cdot\Delta u_{i+\frac{1}{2}} \tag{48}$$

where

$$\begin{cases} \Delta u_{i-\frac{1}{2}} \equiv u_i^{\mathrm{n}} - u_{i-1}^{\mathrm{n}} \\ \Delta u_{i+\frac{1}{2}} \equiv u_{i+1}^{\mathrm{n}} - u_i^{\mathrm{n}} \end{cases} \tag{49}$$

And ω is a free parameter in the real interval $[-1, 1]$.

2.2.5 TVD of MUSCL-Hancock scheme

Total variation diminishing (TVD) schemes are often employed to further suppress oscillations in regions where nonsmooth solutions are present. The TVD version of the MUSCL-Hancock scheme has a stable second-order accuracy in both time and space, and more importantly, it is oscillation-free. In this section, we construct non-linear versions of these schemes by replacing the slopes Δ_i in the data reconstruction step with limited slopes $\overline{\Delta_i}$, according to some TVD constraints.

$$u_i(x) = u_i^{\mathrm{n}} + \frac{(x - x_i)}{\Delta x}\Delta_i, x \in [0, \Delta x] \tag{50}$$

Based on the theorem, if the limited slopes $\overline{\Delta_i}$ are chosen then the resulting MUSCL scheme is TVD. The slope vector r plays an important role in the scheme, and we can also set slope limiter $\varepsilon(r)$ to limit Δ_i:

$$\overline{\Delta_i} = \varepsilon_i \Delta_i \tag{51}$$

And Δ_i is given by

$$\Delta_i = \frac{1}{2}(1+\omega)\cdot\Delta u_{i-\frac{1}{2}} + \frac{1}{2}(1-\omega)\cdot\Delta u_{i+\frac{1}{2}} \tag{52}$$

Here, we find Δ_i can lead to a TVD region for $\varepsilon(r)$ (Van Albada et al., 1997):

$$\begin{gathered}\varepsilon(r) = 0 \text{ for } r \leq 0; \\ 0 \leq \varepsilon(r) \leq \min\left\{\varepsilon_{\mathrm{L}}(r), \varepsilon_{\mathrm{R}}(r)\right\} \text{ for } r > 0\end{gathered} \tag{53}$$

Where r is the ratio of slope at the surface of each cell, and

$$\begin{cases} \varepsilon_L(r) = \frac{2r\cdot\beta_{i-\frac{1}{2}}}{1-\omega+(1+\omega)r} \\ \varepsilon_R(r) = \frac{2r\cdot\beta_{i+\frac{1}{2}}}{1-\omega+(1+\omega)r} \\ r = \frac{\Delta_{i-\frac{1}{2}}}{\Delta_{i+\frac{1}{2}}} \end{cases} \tag{54}$$

And

$$\beta_{i-\frac{1}{2}} = \frac{2}{1+c}, \beta_{i+\frac{1}{2}} = \frac{2}{1-c} \tag{55}$$

Where c is the Courant number is a dimensionless value representing the time a particle stays in one cell of the mesh, c is smaller than 1 in our study and we set it as 0.9 in the simulation part; $\beta_{i-\frac{1}{2}}$, $\beta_{i+\frac{1}{2}}$ are coefficients from the scalar case, often simply set as 1.

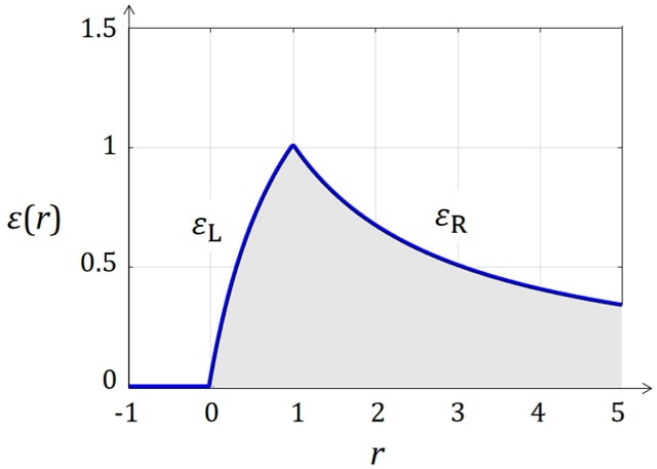

Figure 2.9: TVD region for slope limiters. For negative r, TVD region is single line ε = 0 and for positive r, TVD region lies between 0 and $min\left(\varepsilon_{\mathrm{L}}\left(r\right),\ \varepsilon_{\mathrm{R}}(r)\right)$.

In this study, we choose A van Leer-type slope limiter, which is:

$$\varepsilon(r) = \begin{cases} 0, r \leq 0, \\ \min\left\{\frac{2r}{1+r}, \varepsilon_{\mathrm{R}}(r)\right\}, r > 0 \end{cases} = \begin{cases} 0, r \leq 0, \\ \min\left\{\frac{2r}{1+r}, \frac{2}{1+r}\right\}, r > 0. \end{cases} \tag{56}$$

2.3 Computational time steps

So far, we know how to compute the intercell flux to be used in the conservative formula. The spatial discretization length Δx is chosen on desired accuracy or available computing resources. What remains to be determined is the size of the time step Δt. This is based on the condition. The time step is then given by

$$\Delta t \leq \frac{c\Delta x}{\mathbf{S}^n_{\max}} \tag{57}$$

Where c is the Courant number and $0 \leq c \leq 1$. The closer the coefficient c is to 1, the more efficient the time marching scheme is. $\mathbf{S}^n_{\max}$ is the largest wave speed present throughout at the domain time level n. This means that no wave present in the solution of all Riemann problems travels more than a distance Δx in time Δt.

For the time-dependent, one-dimensional Euler equations a reliable choice is

$$\mathbf{S}^n_{\max} = \max\left\{\left|\mathbf{S}^{\mathrm{L}}_{i+\frac{1}{2}}\right|, \left|\mathbf{S}^{\mathrm{R}}_{i+\frac{1}{2}}\right|\right\} \tag{58}$$

where $\mathbf{S}^{\mathrm{L}}_{i+\frac{1}{2}}$ and $\mathbf{S}^{\mathrm{R}}_{i+\frac{1}{2}}$ are the wave speeds of the left and right non-linear waves present in the solution of the Riemann problem $\mathrm{RP}\left(\mathbf{U}^n_i, \mathbf{U}^n_{i+1}\right)$.

A popular alternative for estimating $\mathbf{S}^n_{\max}$, which extends to multi-dimensional problems, is

$$\mathbf{S}^n_{\max} = \max\left\{|u^n_i| + a^n_i\right\} \tag{59}$$

Only data values for the particle velocity u^n_i and sound speed a^n_i are used here.

Underestimating $\mathbf{S}^n_{\max}$ results in a choice of Δt that is too large, and instabilities may be developed from the beginning of the computations. A possible way of remedying this, is by choosing the CFL coefficient c in cautiously and a practical choice is set $c = 0.9$.

2.4 CUDA

In this study, the entire flow solver is implemented with CUDA programming language and computing platform and runs on a General Purpose Graphics Processing Unit (GPGPU). To achieve high grid resolution simulations and parametric study, the GPU-CPU framework has been used to improve computational performance.

With CUDA, the solutions for all cells are computed separately by every single thread of the GPU. Those threads are logically bonded into blocks and each block components around 64 threads to maintain the capability for inter-thread communication. Up to 512 threads could be executed in parallel on the GPU. By executing multiple blocks at the same time, the GPU can "swap" between blocks and blocks in order to memory delay.

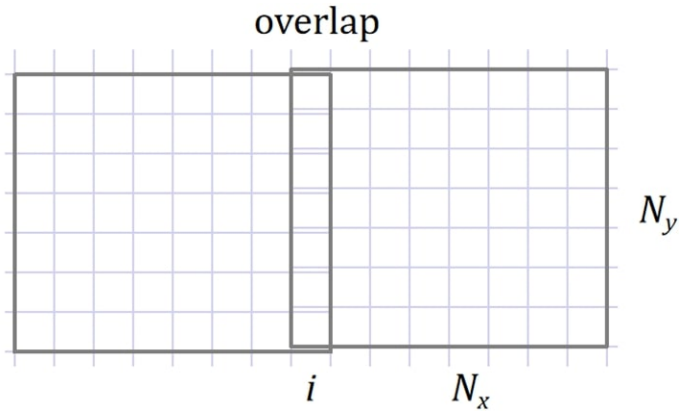

Figure 2.10: Implementation of the Riemann solver using the thread and block configuration with a one-cell overlap between blocks (Morgan, 2013).

To connect all the blocks for the Riemann flow solver, an overlapping cell at the end of each block is required in the solver, as shown in Figure 2.10.

Cells loaded with data $\mathbf{U}_{i-1}$, $\mathbf{U}_i$, and $\mathbf{U}_{i+1}$ reconstruct $\mathbf{U}_i^{\mathrm{L}}$ and $\mathbf{U}_i^{\mathrm{R}}$. Then, the i^{th} cell computes the flux $\mathbf{F}_{i-\frac{1}{2}}$, using the values from reconstructed cell $i-1$ and i. The overlap cannot be computed on the left side of the first block since there is no data available on the left front.

Therefore, the number of blocks that is enough for covering the whole computational system with a designated overlap can be determined by:

$$\text{blocks} = 1 + \left[\frac{\text{grid cells}}{\text{block width} + \text{overlap}} \right] \tag{60}$$

2.5 Code validation

2.5.1 One-dimensional Sod shock tube problem

The HLLC-based solver for the inert (no gas reaction happens), time-dependent Euler equations is validated using the Sod shock tube problem (Sod, 1978) in 1-dimensional, given by initial conditions $q = (\rho, u, p)$; $q_{\mathrm{L}} = (1.0, 0.75, 1.0)$ and $q_{\mathrm{R}} = (0.125, 0.0, 0.1)$. For the ideal gas: $\gamma = 1.4$. This example separates the two sides by discontinuous points at position $x = x_0 = 0.3$. There are also enough cells (1000 cells) in the analytical domain from 0 to 1. The courant number here is 0.9. The solution to this problem after $t = 0.2s$ and 56 time-steps can be seen in Figure. 2.11.

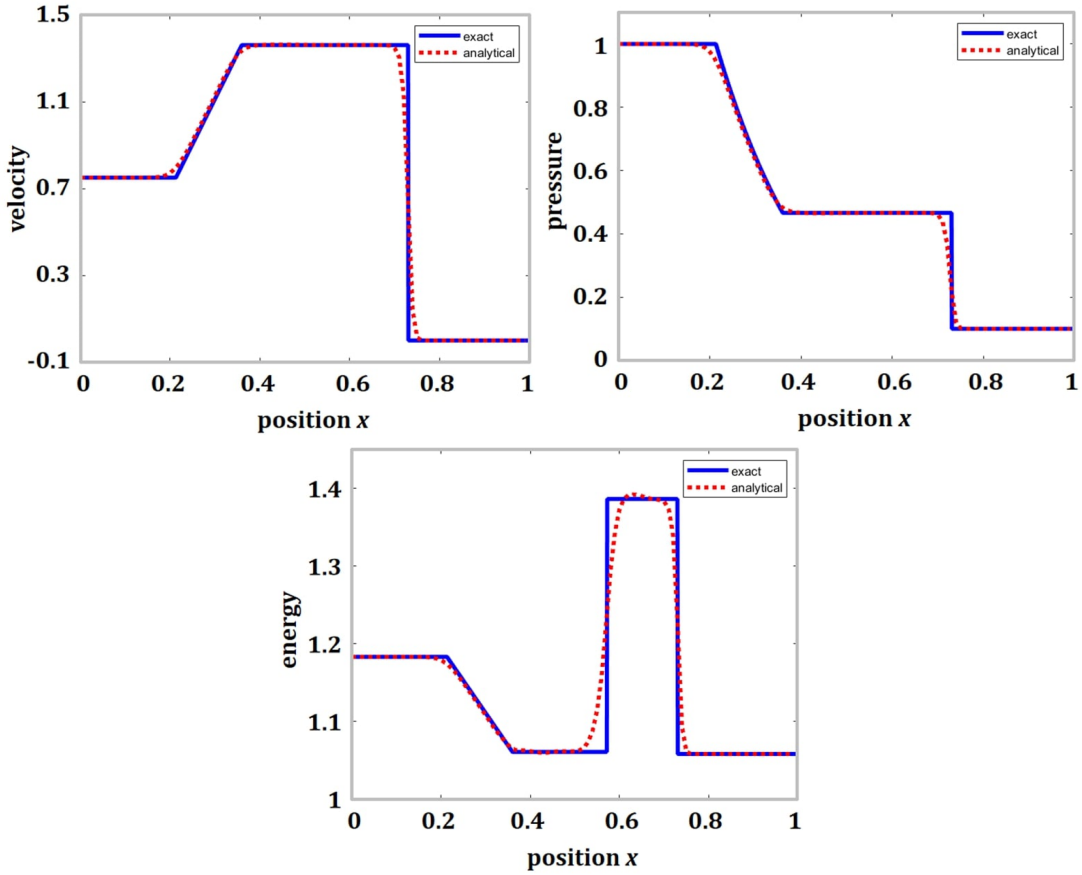

Figure 2.11: Velocity, pressure, and energy plots for exact and approximate solution of Sod's shock tube problem.

From the above figures, the presence of a right shock wave, a contact discontinuity, and a left sonic rarefaction wave can be seen. The solution has a fairly high degree of accuracy, showing general trends in the process and exact values at each stage. The right shock wave, located at $x \approx$

0.73, can be identified since $p_* > p_{\mathrm{R}}$. It is compressive in nature and it results in very rapid changes in physical quantities. The central contact discontinuity is located at a value of $x \approx 0.58$. Velocity and pressure remain constant, while energy changes. (Density increases a lot here causing energy drops.) Finally, the left rarefaction wave is located between $x \approx 0.35$ and $x \approx 0.2$. It can be identified by $p_* \leq p_{\mathrm{L}}$ and there is a smooth transition of velocity, pressure, and energy.

2.5.2 Two-dimensional structure of cellular detonation

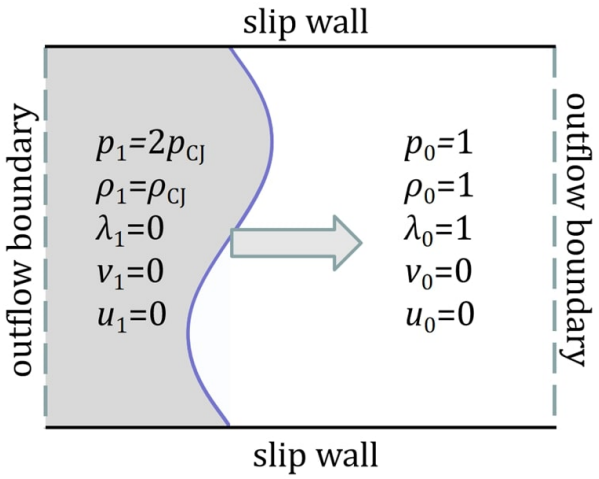

Figure 2.12: The initial and boundary conditions of the simulation.

A numerical simulation of unsteady shock waves in 2-D using a Riemann solver is described. The boundary and initial conditions are shown in the Figure. 2.12. The top and bottom boundaries are reflective, while a constant velocity D_{CJ} inflow is defined at the right boundary. (except for $\beta = 0$)

$$\begin{aligned} \mathbf{U}_{-1} &= (1-r)\mathbf{U}_0 + r\mathbf{U}_{in} \\ \mathbf{U}_{-2} &= (1-r)\mathbf{U}_1 + r\mathbf{U}_{in} \end{aligned} \tag{61}$$

Where $\mathbf{U}_i$ with $i < 0$ represents ghost cells and $r = 0.05$ (Gamezo et al., 1999). In the left boundary, a sinusoidal surface divides the domain into two parts:

$$x = 5\sin\left(\frac{2\pi}{100y}\right) + x_1 \tag{62}$$

An overpressured $2P_{\mathrm{CJ}}$ region was placed in the left half of the domain to initiate a reaction,

resulting in a detonation wave is approximately one-fourth of the 200×100 simulated domain, with 20 grid points per $L_{1/2}$. Although the numerical error can depend on the perturbation of the shock wave, a single-mode perturbation is applied to the shock wave in some simulations to accelerate the convergence to steady-state pulsatile detonation.

Table 2.1: Initial conditions for the cellular detonation simulation.

Parameters	Values
Heat release, Q	50
The ratio of specific heats, γ	1.2
Initial Front position, x_1	50
Post-shock density, ρ_1	1.795
Post-shock pressure, p_1	43.08
CJ detonation pressure, p_{CJ}	21.54
CJ detonation Mach number, M_{CJ}	6.2162

Three cases of different groups of activation energy E_{a} and pre-exponential factor k_{R} are tested, relatively:

$$\begin{aligned} E_{\mathrm{a1}} &= 10, k_{\mathrm{R1}} = 3.7 \\ E_{\mathrm{a2}} &= 20, k_{\mathrm{R2}} = 16.7 \\ E_{\mathrm{a3}} &= 25, k_{\mathrm{R3}} = 36.5 \end{aligned} \tag{63}$$

Soot foil is a regular way to record the cellular structure of detonation in experiments. For the numerical method, recording the maximum pressure that ever existed at each grid cell is a way to reproduce the soot foil.

Figure. 2.13 shows the numerical results of simulated soot at $E_{\mathrm{a}} = 10$. The detonation is caused by an early sinusoidal disturbance and rapidly develops into a stable form of fibrous detonation structure. Late-stage patterns of the cellular structure are also shown. Despite the splitting and combining of shear waves, the pattern of cells remained relatively regular. Therefore, in this case of moderate activation energy, the cellular detonation structure is moderately stable. Cells were similar in size except in the case of shear wave division or combination.

The numerical soot foils obtained with lower $E_{\mathrm{a}} = 20$ and higher $E_{\mathrm{a}} = 25$ are respectively shown in the Figure. 2.14 and 2.15. As we can see, for $E_{\mathrm{a}} = 20$, the soot pattern is more irregular with more cells and the maximum pressure is also considerably higher. In addition, soot foil at the

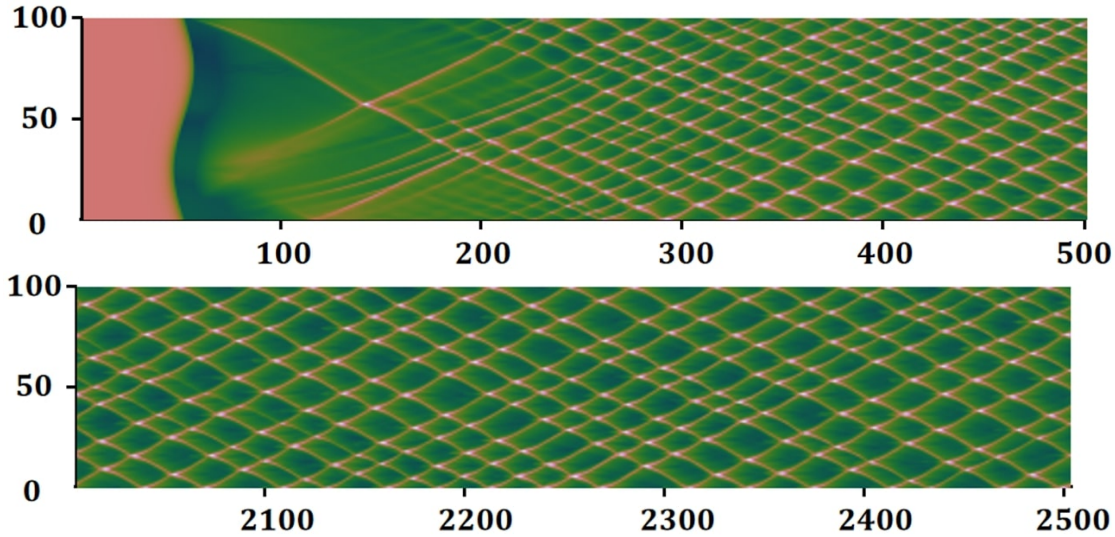

Figure 2.13: Numerical soot foil of $E_{\mathrm{a}} = 10$. The upper figure is the result of early time showing the sinusoidal perturbation and the initiation of detonation; the lower one is the late cellular structure.

high activation energy $E_{\mathrm{a}} = 25$ is full of chaotic interactions with various waves interacting with each other, and the maximum pressure is shown higher.

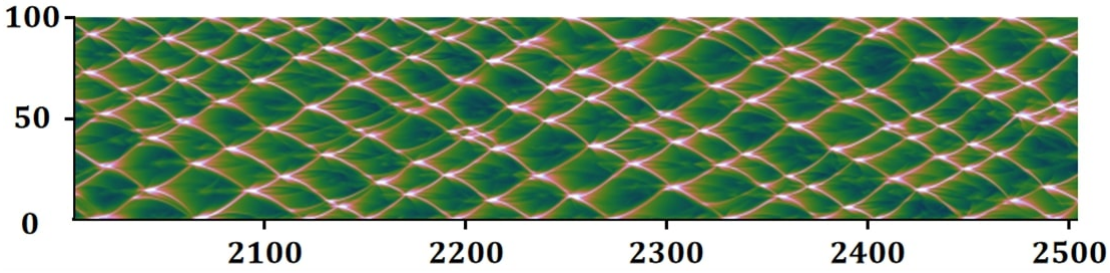

Figure 2.14: Numerical soot foil of $E_{\mathrm{a}} = 20$ at late times, of which the cellular structure becomes irregular.

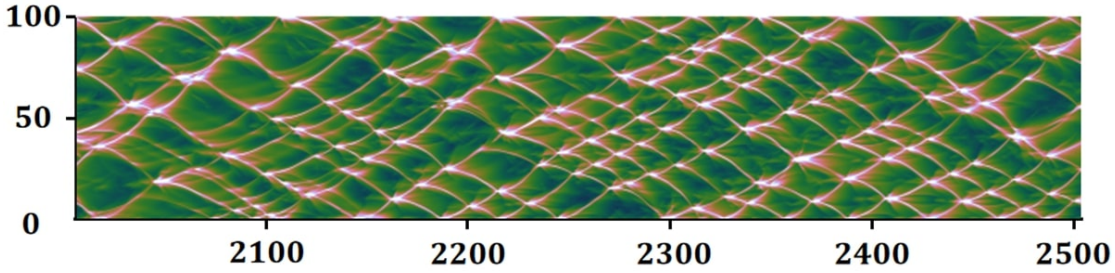

Figure 2.15: Numerical soot foil of $E_{\mathrm{a}} = 25$ at late times, of which the cellular structure is more chaotic.

Figure. 2.16 below also displays an images sequence of density schlieren plots showing the

unstable detonation front of $E_{\mathrm{a}} = 20$ at late times showing transverse waves sweeping across the front and the generation of triple points and wave structure with Mach reflection (incident waves, transverse waves and Mach stem).

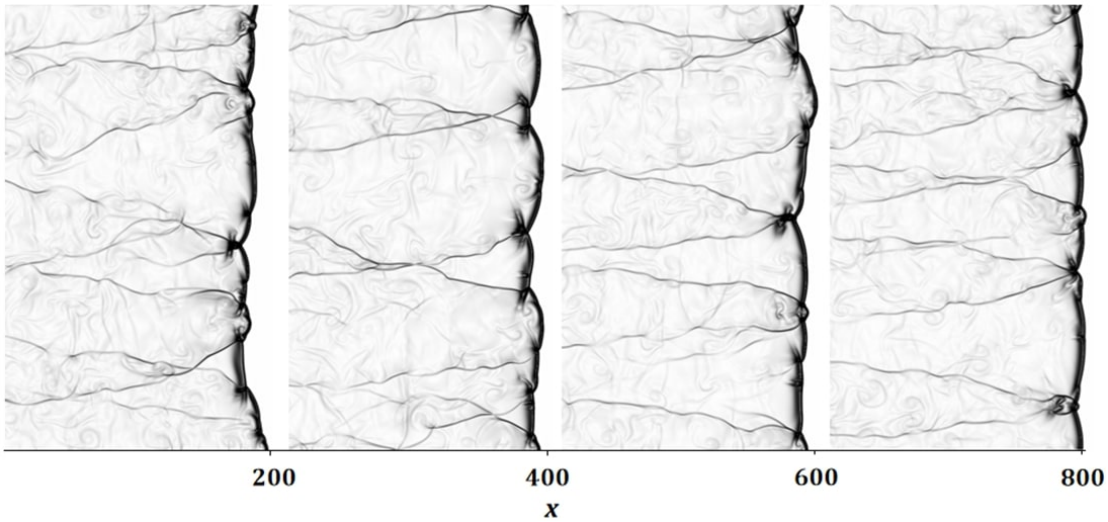

Figure 2.16: A sequence of four density schlieren plots of detonation structure development with $E_{\mathrm{a}} = 20$.

2.6 Grid resolution study

In this slide, two grid resolutions of 10 and 20 points per induction-zone length, are investigated as part of a resolution study. Two grid resolutions of 10 and 20 points per reaction-zone length are

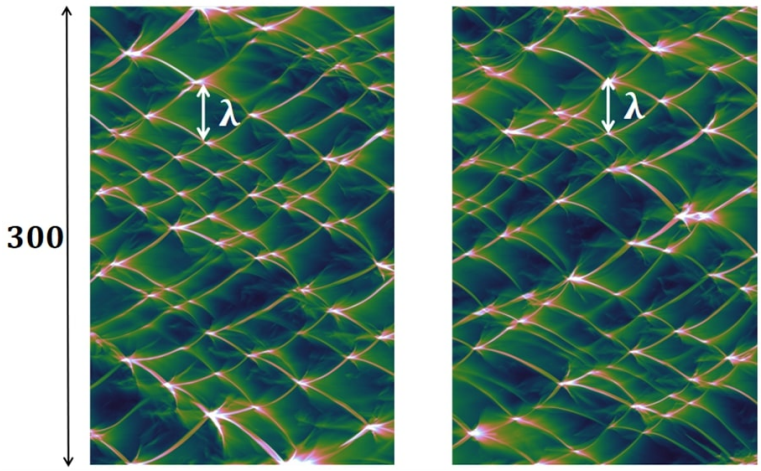

Figure 2.17: Numerical soot foils showing the cellular detonation structure and average cell size γ in a smooth channel obtained with a resolution of 10 (left) and 20 (right) grid points per unit $L_{1/2}$.

investigated as part of a resolution study. Figure. 2.17 shows a parallel comparison of soot foils showing the CJ detonation cell structures in smooth channels under consistent setup obtained with a resolution of 10 and 20 cells per unit $L_{1/2}$. The cell irregularity is qualitatively similar and the cell size λ agrees approximately with each other. By running simulations in both resolutions, the average detonation velocities with both grid resolutions are also similar. By far, considering that this work only aims at qualitative study, a grid resolution of 10 per unit $L_{1/2}$ is thus deemed sufficient and used for all subsequent simulations to accelerate the simulation run time.

2.7 Summary

In this chapter, the mathematical models and equations governing the two-dimensional detonation waves are given. The applicability of the MUSCL-Hancock scheme to the numerical solution of the simulation governing equations is proposed, improving the second-order accuracy where Godunov's scheme cannot be applied. The HLLC approximate Riemann solver is then chosen to solve this problem, which directly calculates the numerical flux between cells, which improves the efficiency of the numerical simulation, and the difference in results is generally negligible compared with the exact Riemann solver. The CFL number criterion is used to select the appropriate time step, which ensures the stability of the time integration algorithm. This study adopts the CUDA computing platform to make full use of computing resources to ensure that they are not wasted while maintaining the accuracy of resolution. The numerical method is verified by the simulation of the one-dimensional Sod shock tube problem and the honeycomb detonation structure.

Chapter 3

Parametric Study of Roughness Effects Induced by Obstacles

Chapter 2 describes the physical reacting flow model and numerical method for detonation simulation. This chapter will focus on the question "How do the cellular dynamics change in rough-walled tubes or for a quasi-detonation wave?" As the tube wall roughness changes, so does the detonation velocity and cell structure, and in order to determine the deterministic effect of roughness on stability, A variation in cellular dynamics of quasi-detonations is considered by performing multiple simulations for each value of roughness to examine the failure or not. To do this research, a 2-D numerical simulation is carried out using a second-order finite-volume model with an inviscid Euler equation.

The numerical soot foils for the smooth and rough-walled channels are the focus of this work showing the corresponding features of the designated initial numerical setup. The numerical soot foils record the maximum pressure to present the trajectory of high-pressure triple points in the detonation front, giving us a visual image of the cellular detonation structure in a two-dimensional plane.

3.1 Computational setup

In order to represent a three-dimensional rough tube as a two-dimensional channel, a schematic of the computational setup with an incident detonation wave initially propagating in a smooth channel is shown in Fig. 3.1 A symmetric boundary condition was applied to the top boundary and hence, $D_{1/2}$ represents only half of the channel width. The exact computational domain is shown in the red dashed box. The left and right boundaries of the domain were transmissive, and the bottom boundary is a wall boundary. Uniform rectangular obstacles are arrayed along the bottom boundary to mimic and adjust the wall roughness. The incident cellular detonation wave in the smooth channel is first simulated separately with a very long channel length, allowing it to fully develop. An advancing-window technique (Teodorczyk et al., 1989) is used in this study to reduce the use of data memory and optimize computational time for simulating detonation waves propagating over a long distance. The length of the computational domain is 400 and the height of that is $D_{1/2} = 200$ or 300, so the computation domain is a rectangle with a mesh size of 400×200 or 400×300. As indicated in Fig. 3.1, the obstacle size is $\alpha \times n\alpha$, where the width of the obstacle is fixed at $\alpha = 25$, and the obstacle height factor is $n = 1$, 2 and 3. The distance between two consecutive rectangular obstacles l is fixed at four times the side length, i.e., $l = 4\alpha$. In this study, the obstacle height factor n plays a main role in altering the obstacle size and wall roughness.

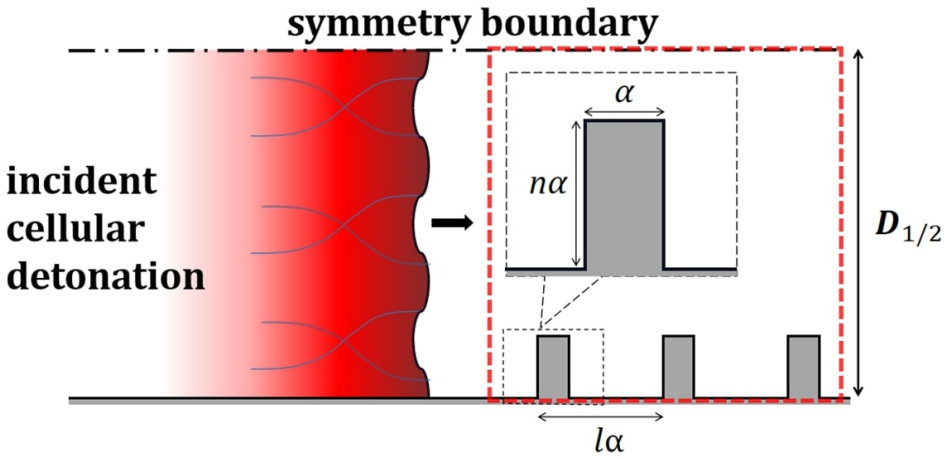

Figure 3.1: Schematic of an incident detonation wave propagating into a rough-walled channel and the computational domain (red dashed box).

After fully developing in a smooth tube, the cellular detonation wave propagates into a rough-walled channel where the uniform rectangular obstacles are arrayed along the bottom boundary to mimic and adjust the wall roughness, where the ratio of roughness increment to tube diameter $\alpha/D = 0.0625$ is small enough to present roughness changes.

In this study, the same dimensionless thermodynamic parameters of the combustible mixture as in Yuan et al.(2021, 2022) are considered.

Table 3.1: Mixture parameters and corresponding CJ detonation properties.

Parameters	Values
Heat release, Q	21.365
The ratio of specific heats, γ	1.32
Post-shock temperature, T_s/T_0	5.0373
Activation energy of the thermally neutral induction process, E_{I}/T_s	5.414
Activation energy of the exothermic reaction, E_{R}/T_s	1.0
The pre-exponential factor of the induction step, k_{I}	1.0022
The rate constant for the heat release, k_{R}	$1.0, 2.0, 4.0$
The Chapman–Jouguet (CJ) detonation velocity, V_{CJ}	5.858

These thermodynamic properties approximately represent the Zel'dovich-von Neumann-Doring (ZND) detonation structure of the stoichiometric hydrogen-oxygen mixture at 20kPa and 300K, giving rise to an unstable CJ detonation wave with a relatively irregular cellular pattern.

3.2 Comparison between smooth and rough channels

From previous research, we know that detonation dynamics are sensitive to boundary conditions (Lee, 2008). In a smooth tube, the detonation velocity is a unique Chapman-Jouguet velocity and the velocity loss is approximately neglectable. When a gaseous detonation wave propagates in a rough-walled tube, its velocity could be less than the Chapman-Jouguet value due to losses of confinement. This propagation regime is usually referred to as quasi-detonation. From the fundamental perspective, investigating both the quasi-detonation propagation and its flow structure could reveal some significant insights into the dynamics of how instabilities affect detonation dynamics.

First, the soot foils as well as the wave velocity evolution for both the smooth and rough-walled tube cases are shown for comparison, see Figs. 3.3 and 3.4. For the quasi-detonation one, the

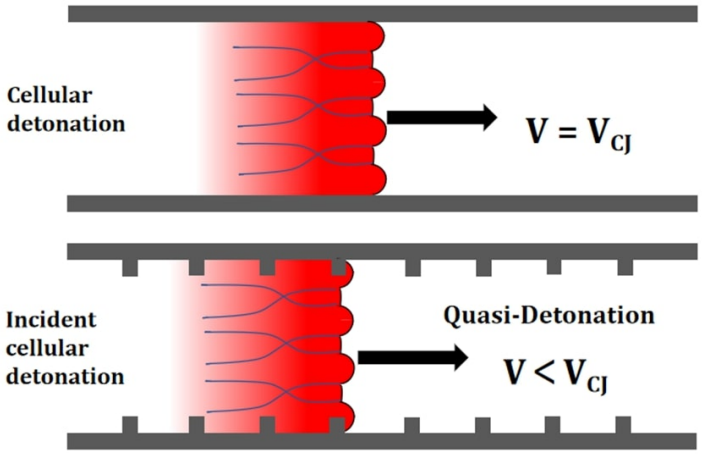

Figure 3.2: Smooth and rough-walled tube models.

variable properties are $k_{\mathrm{R}} = 1, n = 1, l = 4, D_{1/2} = 300$.

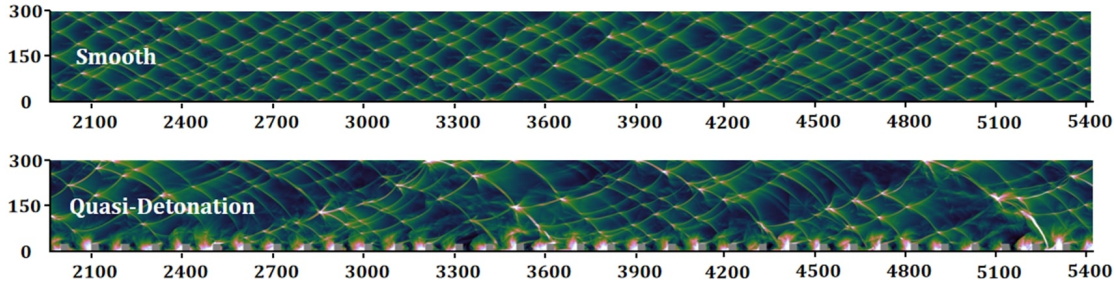

Figure 3.3: Soot foils showing cellular patterns of detonations in a smooth channel with $D_{1/2} = 300$ and $k_{\mathrm{R}} = 1$ in the upper figure, the below one is the quasi-detonation with obstacle height $n = 1$.

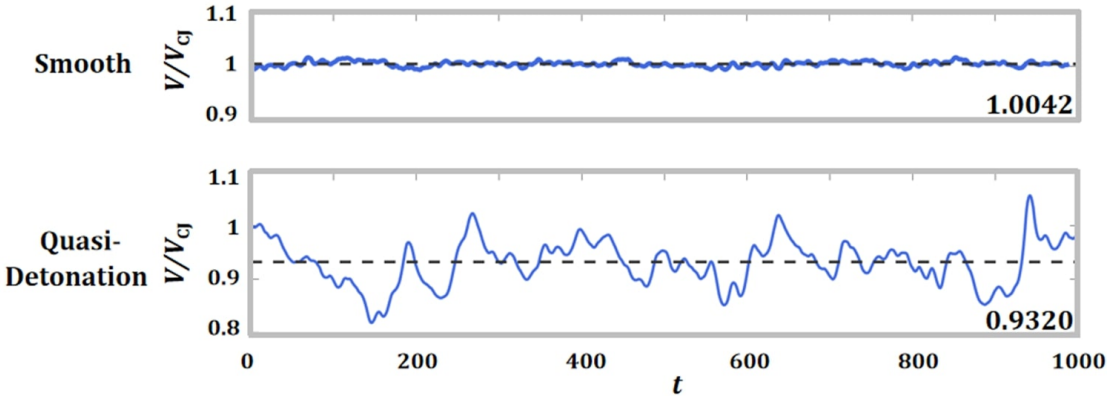

Figure 3.4: Time-dependent transient velocity evolution (blue line) when $k_{\mathrm{R}} = 1$ and average velocity in a smooth tube as well as propagating in rough-walled channels with obstacle height $n = 1$.

For the smooth tube case, the detonation propagates essentially at a velocity close to the CJ value, $V/V_{\mathrm{CJ}} \sim 1.0042$. When roughness is introduced in the tube, e.g., with n = 1, the average normalized velocity decreases to 0.932. With the momentum loss in the propagating direction, the quasi-detonation has a wave velocity less than the ideal CJ velocity. And when we add some roughness in a tube, like $n = 1$, the average velocity of the quasi-detonation propagation is 0.932 which is less than the CJ velocity.

3.3 Effect of different widths in smooth and rough tubes

We fix the pre-exponential factor $k_{\mathrm{R}} = 4$, then change half channel widths, $D_{1/2} = 200$ and 300. In Figure. 3.5, one can say the cellular structures in both soot foils remain relatively regular. The channel width in a moderate magnitude has thus very little effect on detonation cell patterns and the detonation cell sizes.

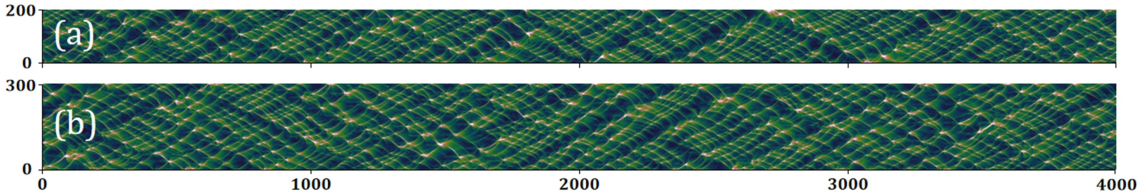

Figure 3.5: Soot foils showing cellular patterns of CJ detonations at $k_{\mathrm{R}} = 4$ in smooth channels with different half channel widths: (a) $D_{1/2} = 200$ and (b) $D_{1/2} = 300$.

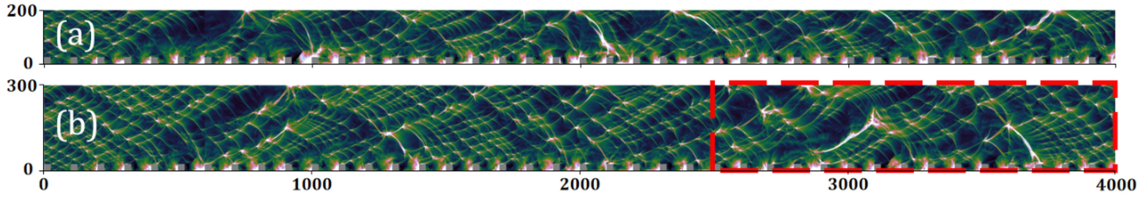

Figure 3.6: Soot foils showing cellular patterns of quasi-detonations at $k_{\mathrm{R}} = 4$ in rough-walled channels with obstacle size $n = 1$: (a) $D_{1/2} = 200$ and (b) $D_{1/2} = 300$.

When the obstacles of the same height $n = 1$, i.e., the size of obstacles is 25×25, are added to the bottom boundary in a uniform sequence to mimic a rough wall, irregularities are introduced to the flow field due to the perturbation from the obstacles, leading to a more chaotic pattern of the cellular detonation structure. In Fig. 3.6, one can see the cellular pattern in (a) is more irregular and the cell size λ is larger than that of (b). This is reasonable since the blockage ratio of (a) is

$n\lambda/D_{1/2} = 1/8$ and that of (b) is $n\lambda/D_{1/2} = 1/12$. For lower channel widths, the wave reflections between obstacles and walls bring more irregularities to the whole flow field. When the width of the domain, which is the half channel width $D_{1/2}$ in this study, equals over 200 for this chemical parameter setup, $D_{1/2}$ is greater than 7λ. The regions near the bottom boundary are more affected as compared to the center of the channel, which corresponds to the top boundary in this work.

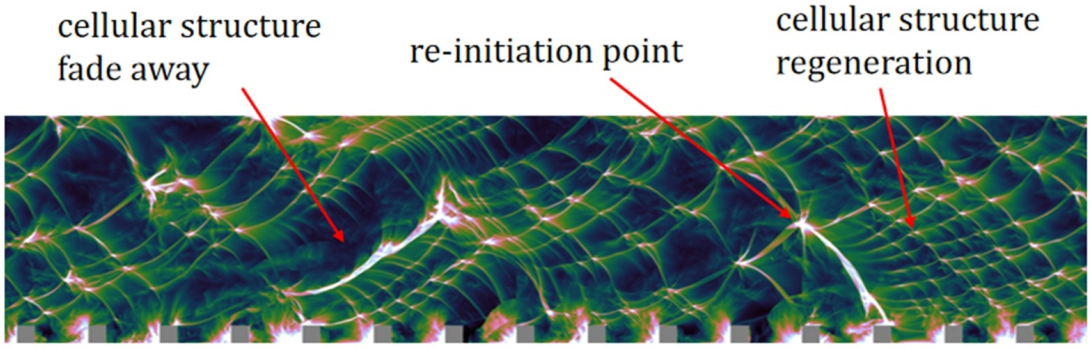

Figure 3.7: A sample numerical soot foil showing the computational setup and the cellular detonation pattern in a rough-walled channel.

Focusing on the region bounded by the red dashed lines in Fig. 3.6 (b), we can detail various flow features in the flow field. The instabilities resulting from the rough walls cause cell size irregularities, local failure with the disappearance of detonation cells, and re-initiation points generating new cellular structures.

3.4 Effect of the rate constant of heat release k_{R}

This section analyzes the soot foils with three different k_{R} values with $D_{1/2} = 300$ and $n = 1$, while the half diameter of the tube and roughness are fixed.

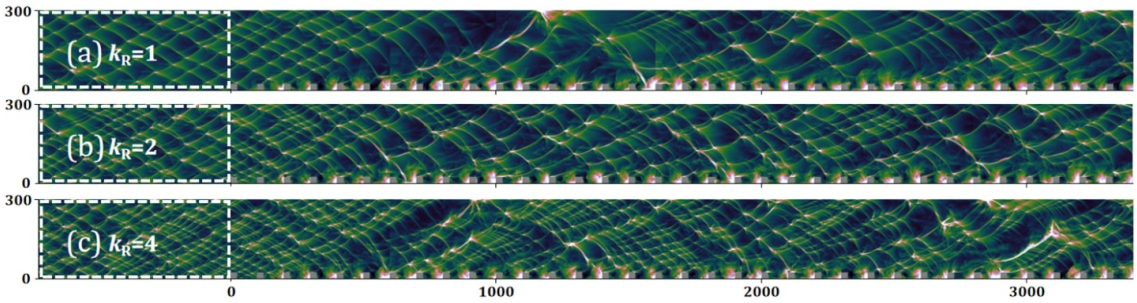

Figure 3.8: Soot foils showing cellular patterns of quasi-detonations in rough-walled channels with $D_{1/2} = 300$, obstacle height $n = 1$, and (a) $k_R = 1$, (b) $k_{\mathrm{R}} = 2$ and (c) $k_{\mathrm{R}} = 4$. The dash-lined boxes display the incident CJ detonation patterns.

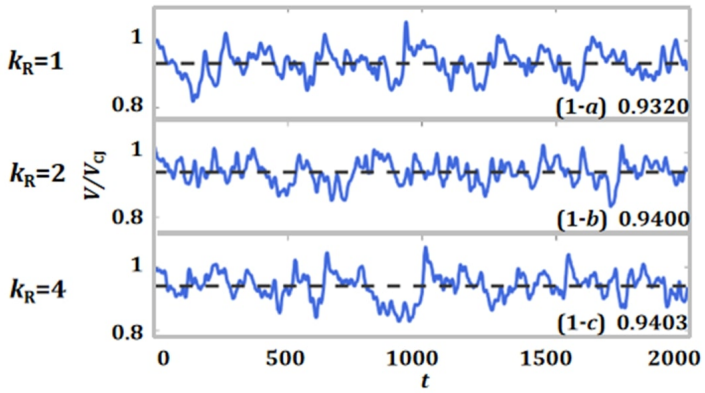

Figure 3.9: The average velocity ratio V/V_{CJ} within a given time range (from 0 to 2000) with a grid of resolution 10 points per unit $L_{1/2}$, domain 400×300, with different pre-exponential factors k_{R} and different roughness factors n (obstacle size): (a): $k_{\mathrm{R}} = 1, n = 1$ (obstacle 25×25); (b): $k_{\mathrm{R}} = 2, n = 1$; and (c): $k_{\mathrm{R}} = 4, n = 1$.

Displayed in the dash-lined boxes is the incident Chapman-Jouguet detonation wave pattern. With lower k_{R}, $k_{\mathrm{R}} = 1$, the incident detonation is relatively stable while with an increase of k_{R}, the detonation becomes more unstable, and the irregular cells also become smaller. This is due to the chemical reaction process being more sensitive to the heat release with the increase of the pre-exponential factor k_{R} in the Arrhenius equation. After a period of propagation, this inherent feature brought by the chemical reaction is translated into the corresponding quasi-detonation cell structures in a rough-walled channel. As a result of this part, the feature of various k_{R} is mostly observed on the soot foil figures instead of the average velocity graphs.

3.5 Effect of roughness factor *n*

By fixing the half channel width at $D_{1/2} = 300$ and the pre-exponential factor at $k_{\mathrm{R}} = 4$, altering the obstacle height gives a clearer demonstration of the effect of the artificial geometric perturbation on the quasi-detonation structure.

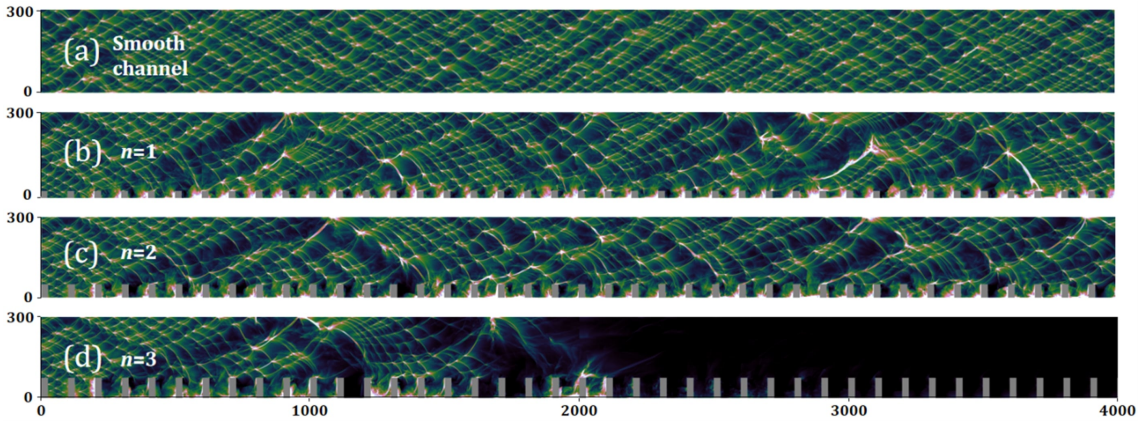

Figure 3.10: Soot foils showing cellular patterns of detonations in channels with $D_{1/2} = 300$ and $k_{\mathrm{R}} = 4$, (a) smooth channel, (b) $n = 1$, (c) $n = 2$ and (d) $n = 3$.

Fig. 3.10 (a) gives a cellular structure of the CJ detonation propagating in a smooth channel as a reference. As shown in (b) and (c), i.e., the rough-walled cases with obstacle height factors $n = 1$ and 2, the cellular patterns are disturbed, and cells are enlarged in some regions while relatively unperturbed cells remain in some other parts of the channel.

Some high-pressure triple point tracks appear after the enlarged cells, showing weak local explosions due to the irregularities caused by the obstacles. The cell sizes of quasi-detonations in rough-walled channels are thus greater than those resulting from a smooth channel. At an overall level, for a relatively small value of n, i.e., $n = 1$ or 2, the cellular frontal structure of the quasi-detonation is retained. In other words, the presence of the wall roughness only generates small perturbation and induces irregularity in the cellular quasi-detonation front. No decoupling process of the leading front from the reaction zone is found and the cell enlargement is at a moderate level.

By further increasing the obstacle size to $n = 3$, the strong perturbation from the larger geometric scale of the obstacles at the wall becomes significant for the quasi-detonation propagation

dynamics. In (d), triple point tracks in the numerical soot foils and cell structures completely vanish. There are no new detonation cells regenerated after the vanished region, which indicates there is no typical strong local explosion or abrupt re-initiation. The losses caused by strong perturbation from larger-scale obstacles eliminate the detonation frontal structure, hence causing failure. The detonation structure and its dynamics are different from the quasi-detonations shown in previous figures and are dominated by the presence of each discrete obstacle. The obstacles change the overall propagation mechanism and the reflections from the obstruction lead to a quasi-detonation. This is usually a consequence of the weakly decoupling of the detonation front and the reaction zone, and the effects distribute upward towards the center core.

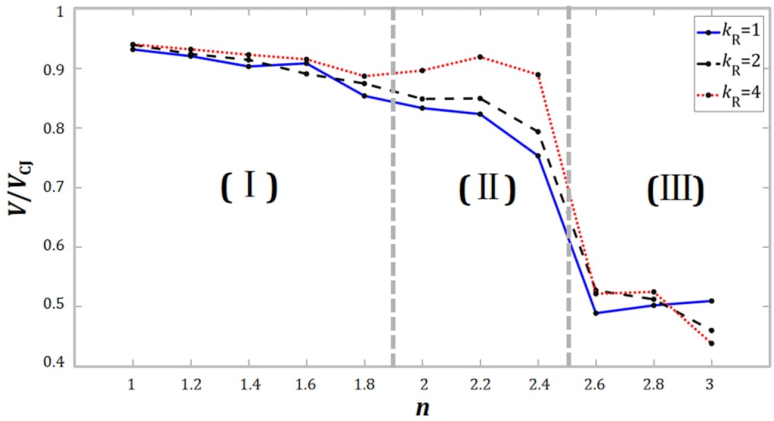

Figure 3.11: The relationship between average velocity and roughness factors n of detonation propagation in channels with $D_{1/2} = 300$ and heat release constant $k_{\mathrm{R}} = 1, 2, 4$. (Ignoring the smooth part causing their average velocity to be approximately V_{CJ}, makes $V/V_{\mathrm{CJ}} = 1$)

Fig. 3.11 shows the normalized average velocity for different roughness levels and pre-exponential factors k_{R}. In general, it is clear that the higher the roughness, with increasing n, the higher the velocity deficit with lower V/V_{CJ}. Fig. 3.12 also demonstrates that with increasing roughness, the local propagating velocity fluctuates significantly. The graph above is separated into three parts, for part (I), the propagation is relatively stable with an average frontal detonation velocity of approximately $0.9V_{\mathrm{CJ}}$. In the second part (II), the average velocity of the detonation turns out to be random, but overall continues to decrease as n increases. For most conditions, after a re-ignition place, the decoupled cellular structure in the soot foil will continue developing in a quasi-detonation

mode. The average velocity ratio is about 0.8. In part (III), the cellular structure in the soot foil of detonation propagation decoupled because of the high roughness factor, then no re-ignition occurs. The average velocity ratio after decoupled is around 0.5 for all the cases.

After all, the critical value for the failure of detonation propagation is found to be about $n = 2.5$. For another case in which the propagation remains relatively stable is about $n = 1.9$.

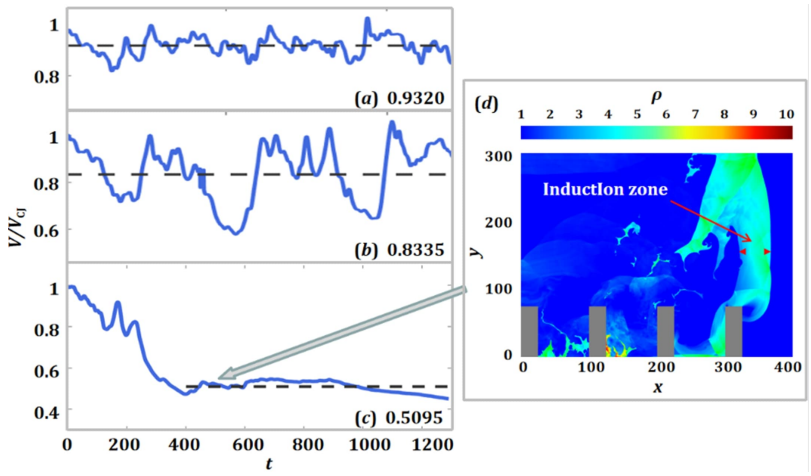

Figure 3.12: Left part is the average velocity ratio V/V_{CJ} within a given time range (from 0 to 1200) with a grid of resolution 10 points per unit $L_{1/2}$, domain 400×300, with different roughness factors n; Right part is a transient frame of this relatively "steady" state shown in the density contour.

For the conditions when $n = 3$, the detonation velocity drops rapidly after a short period of strong fluctuation and ends at a relatively steady state after around $t = 400$ to 800, and after the decoupling, the velocity of the frontal shock wave propagates at $0.4V_{\mathrm{CJ}}$ to $0.5V_{\mathrm{CJ}}$. In Figure. 3.12, the density contour displays the decoupling process of the leading shock and chemical reaction zone.

3.6 Effect of length between two obstacles *l*

In this part, we keep other variable properties unchanged, then observe the differences when we vary the length between two obstacles. First, we consider the case keeping the heat release constant $k_{\mathrm{R}} = 1$ and the roughness factor $n = 1$, and the results are shown in Figs. 3.13 and 3.14. From the velocity plots, one can say that when the length between two obstacles is extremely small, which

influences the detonation wave propagating into the recess between the obstacles, we can treat the rough surface as a wall formed by the upper surface of the obstacles. Therefore, the perturbation caused by the roughness turns out to be tiny to influence the propagation.

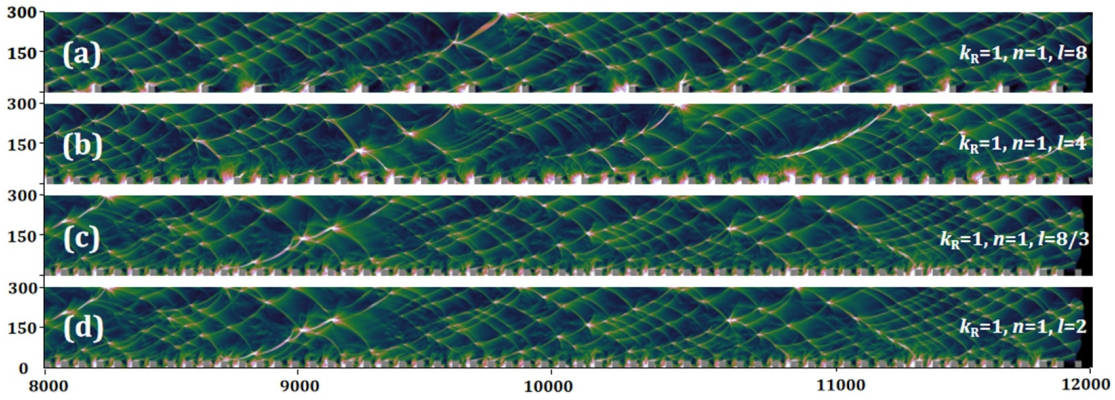

Figure 3.13: Soot foils showing cellular patterns of detonations in channels with $D_{1/2} = 300, k_{\mathrm{R}} = 1$, and $n = 1$, the length factor $l = 8, 4, 8/3$ and 2, respectively.

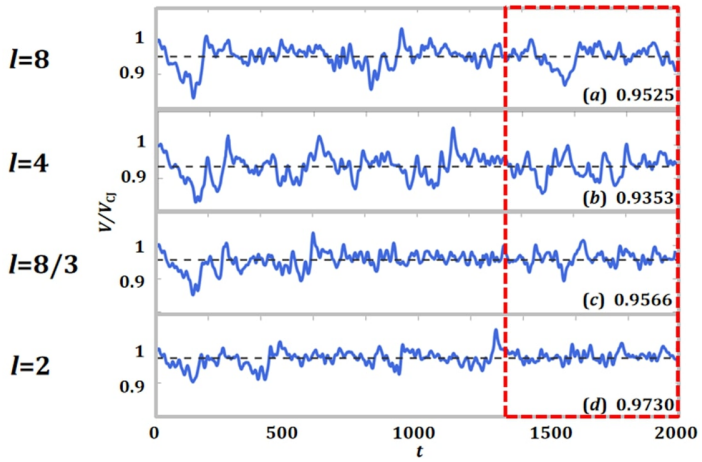

Figure 3.14: The average velocity ratio V/V_{CJ} within a given time range (from 0 to 2000) with a grid of resolution 10 points per unit $L_{1/2}$, domain 400×300, with different length factors l.

But obviously, in these cases, the value of k_{R}, as well as n, are relatively small, and no large perturbation occurs. As a result of that, we change the value of heat release constant k_{R} as well as the roughness factors n to observe more conditions and conclusions.

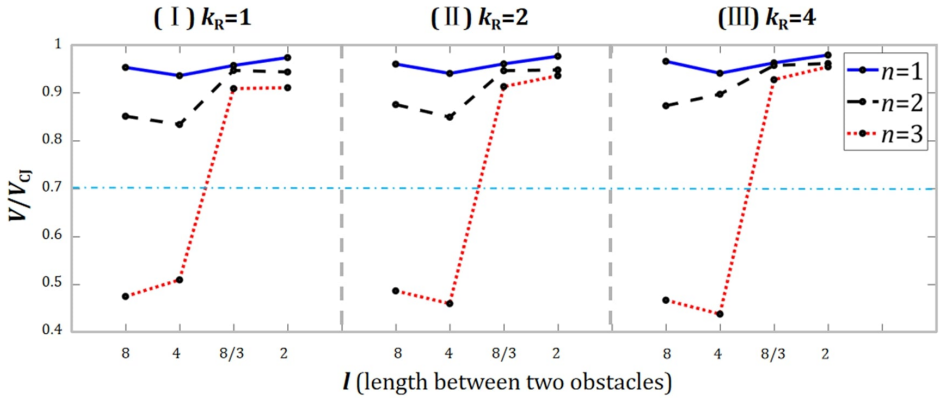

Figure 3.15: The relationship between average velocity and the length between two obstacles l for detonation propagation in channels with $D_{1/2} = 300$ and heat release constant $k_{\mathrm{R}} = 1, 2, 4$ and the roughness factors $n = 1, 2, 3$.

For most cases in Figure. 3.11, the quasi-detonation propagates in a "steady" way, with an average speed of about $0.9V_{\mathrm{CJ}}$. When the length between two obstacles $l = 4$, the average frontal wave speed of the propagation has the lowest values which means getting the biggest influenced by the roughness. When we further decrease the length between two obstacles l to 2, the velocity of the frontal wave speed of the detonation keeps increasing, which means when the obstacles are close enough to each other approaching to a solid wall, the influence is little.

For the cases where the roughness factor $n = 3$, when we make the length between two obstacles $l = 8$ and 4, like the previous ones, the detonation velocity drops rapidly after a short period of strong fluctuation and ends at a relatively steady state after around $t = 400$ to 800, and after the decoupling, the velocity of the frontal shock wave propagates at $0.4V_{\mathrm{CJ}}$ to $0.5V_{\mathrm{CJ}}$. This represents the propagation of the detonation wave is strongly influenced by the rough walls and subsequently fails to propagate in a quasi-detonation form under these cases.

3.7 Effect of different initial conditions

For verification purposes, we choose different initial conditions to ensure these do not influence the observations described in previous sections, i.e., to confirm that scenarios with large roughness will lead to global failure of quasi-detonations in rough-walled channels, and the large deficit in

detonation velocity is not a coincidence.

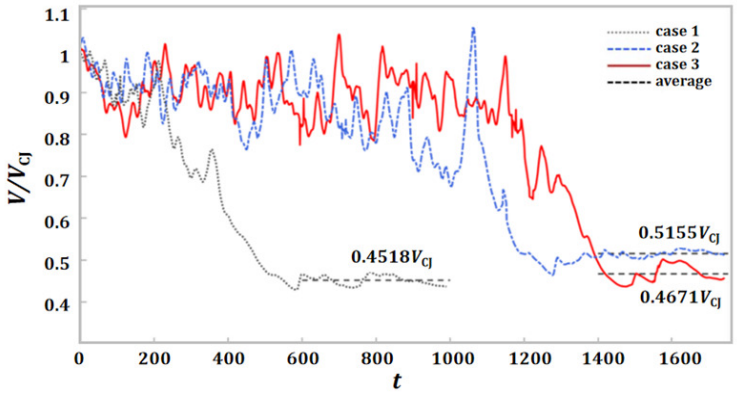

Figure 3.16: Time-dependent transient velocity evolution and average velocity of the quasi-detonation propagating in rough-walled channels with $n = 3$, using different incident CJ detonation waves.

By replacing the cellular patterns of the incident detonation wave with some other random transient frames, the outcomes shown in Fig. 3.12 (c) are repeated with different initial conditions to validate any effects of the initial randomness. In Fig. 3.16, the red and blue lines show another two cases in which the initial incident wave patterns are randomly chosen from the incident detonation timeline. After a long period of strong oscillation, both cases 2 and 3 end at relatively steady states, and $V/V_{\mathrm{CJ}} \approx 0.4 \sim 0.5$ just like case 1. The scenarios with large-scale obstacles such as $n = 3$ will lead to a global failure of the quasi-detonation in rough-walled channels, and the great detonation velocity deficit is not of coincidence.

Chapter 4

Comparison between Staggered and Aligned Obstacle Configurations

4.1 Computational setup

This part of the simulation is under the same conditions as 3.1, only changing the position of obstacles in the channels, i.e., changing them from aligned to staggered, and then observing the evolution of quasi-detonation and failure.

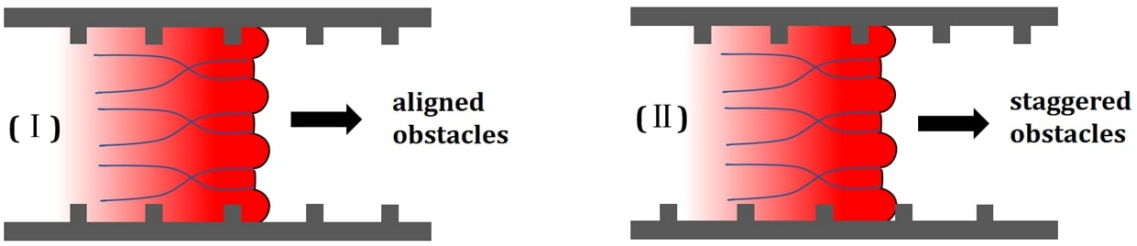

Figure 4.1: The model of previous aligned obstacles rough wall in (I) and the model of staggered obstacles rough wall in this part in (II).

We compare the relationship between the aligned obstacles tubes and the staggered tubes using models like those in Figure. 4.1. To design the model, we also set the obstacles as $n\alpha$ times α on the symmetric boundary, and the distance between two adjacent obstacles on the upper and lower walls is the same on the x-axis.

Because the simulation area has changed from half the tube diameter $D_{1/2}$ to the entire channel diameter D, the computational domain size should also be enlarged from 300×400 to 600×1200 or more to meet the calculation needs. However, to reduce the simulation run-time, the calculation cost should be kept as low as possible. To balance the numerical requirement and the cost, the incident detonation we select has an average cell size over tube diameter $\lambda/D = 0.0606$.

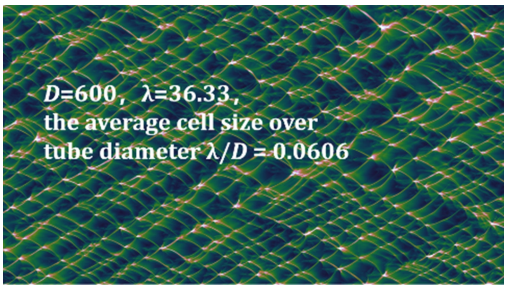

Figure 4.2: The soot foil of the incident detonation with the domain 600×800 and heat release constant $k_{\mathrm{R}} = 4$.

4.2 Soot foil comparison

Keeping other conditions unchanged, we only change the rough factor n and get two sets of graphs in Figs. 4.3 and 4.4. The k_{R} is the highest, resulting in an incident detonation more unstable and a reaction rate more sensitive to temperature perturbation.

Both the cellular structure looks similar, after the detonation propagating for a time period, the cell structure begins to vanish. After that, a reignition point occurs at about a 1500-to-2000 time scale. This process resembles that of Galloping Detonation. (A detonation that periodically fails and reinitiates during propagation. This type of detonation is typically observed in near-limit mixtures (Gao, Ng, & Lee, 2015).)

The galloping cycle includes a relatively long low-velocity phase during which the shock is planar without any cell structure and the reaction front trails behind. It follows by an abrupt re-initiation process resulting in an overdriven wave, which subsequently relaxes to begin a new galloping cycle.

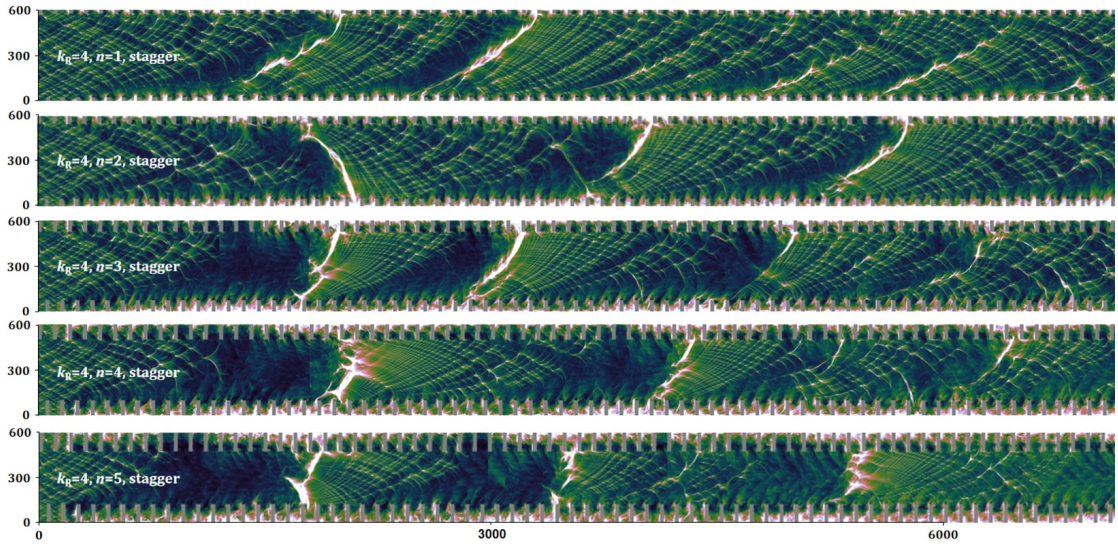

Figure 4.3: Soot foils showing cellular patterns of detonations in staggered obstacles with $D_{1/2} = 300, k_{\mathrm{R}} = 4$, and $n = 1, 2, 3, 4, 5$, respectively.

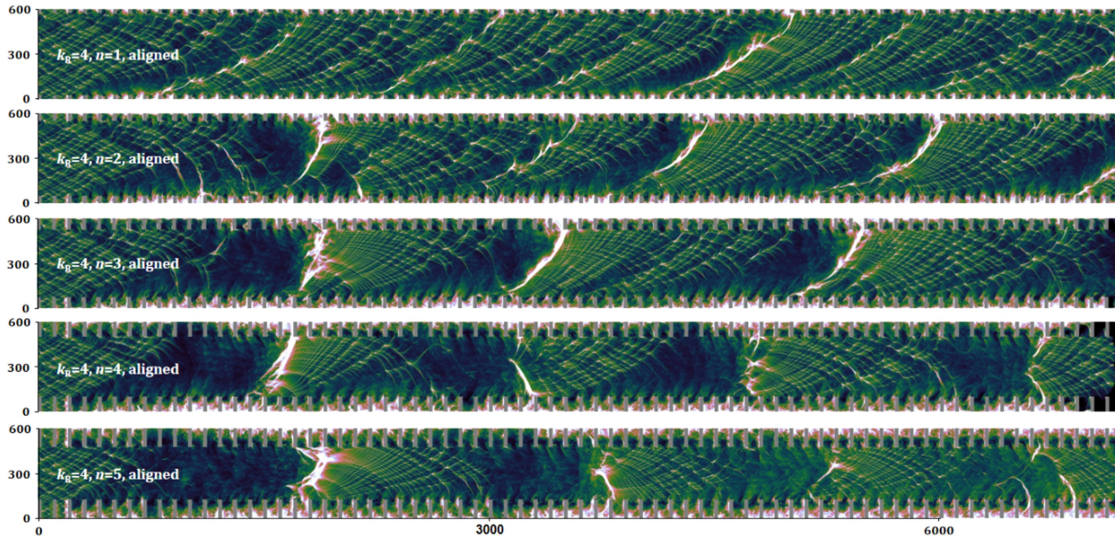

Figure 4.4: Soot foils showing cellular patterns of detonations in aligned obstacles with $D_{1/2} = 300, k_{\mathrm{R}} = 4$, and $n = 1, 2, 3, 4, 5$, respectively.

4.3 Velocity comparison

In this part, we sorted out ten cases of frontal shock average velocity with different roughness factors n of channels with staggered and aligned obstacles. Through the Figs. 4.5 and 4.6, it is not

difficult to find that except for the case of roughness factor $n = 1$, other speed trends are in line with the trend of Galloping detonation, that is, periodic decoupling first and then re-ignition. Through the speed graph, we found that the speed range will become larger with the increase of the roughness factor n, which has no relationship with the tubes of staggered and aligned obstacles. When $n = 2$, $0.6 \leq V/V_{\mathrm{CJ}} \leq 1.1$, and when n increases to 5, $0.2 \leq V/V_{\mathrm{CJ}} \leq 1.2$.

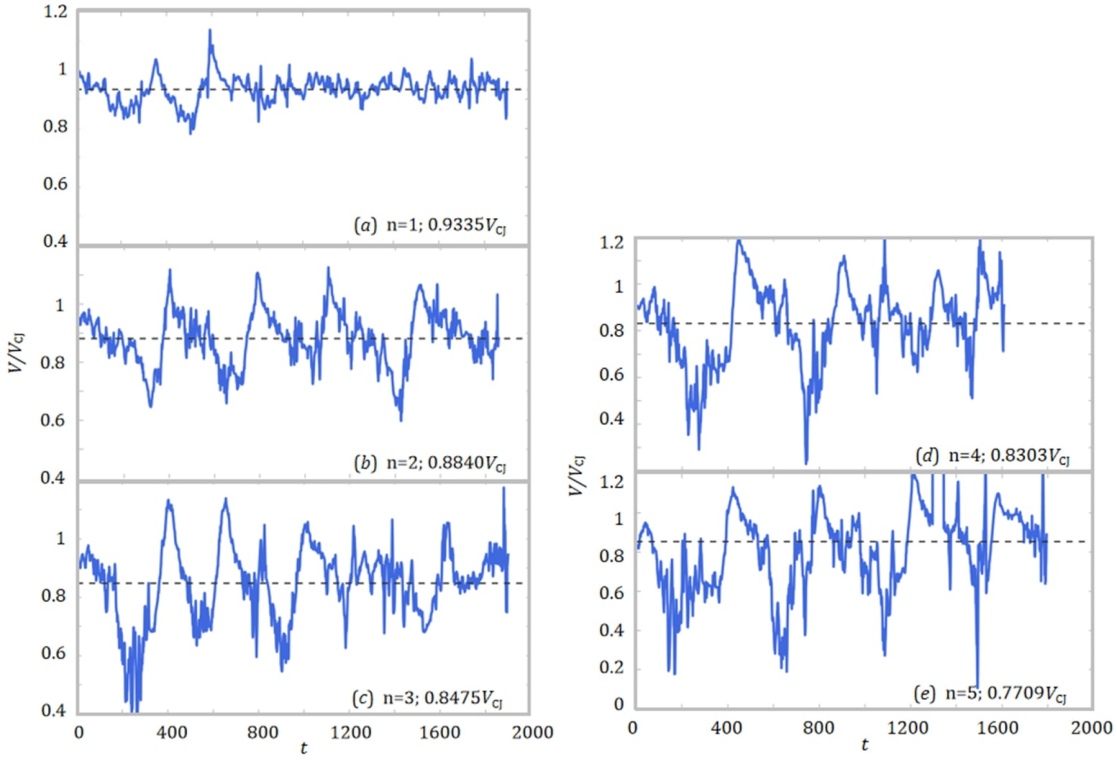

Figure 4.5: Time-velocity ratio graphs showing cellular patterns of detonations in channels with staggered obstacles for $D_{1/2} = 300$, $k_{\mathrm{R}} = 4$, and $n = 1, 2, 3, 4, 5$, respectively.

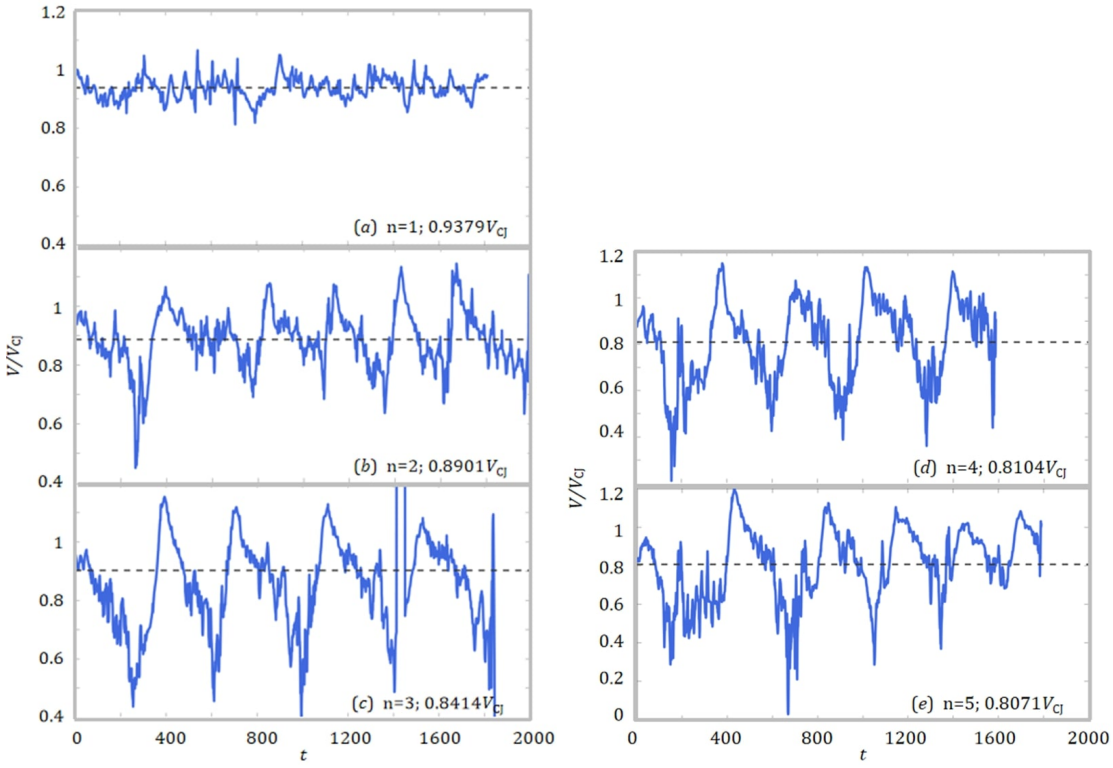

Figure 4.6: Time-velocity ratio graphs showing cellular patterns of detonations in channels with aligned obstacles for $D_{1/2} = 300, k_{\mathrm{R}} = 4$, and $n = 1, 2, 3, 4, 5$, respectively.

The frontal wave velocity of the detonation for these cases has also been calculated, to observe more conveniently, we counted the average speed graph of these cases, see Figure. 4.7.

According to our results, it can be seen that as the roughness factor n increases, the average velocity of the frontal shock velocity decreases uniformly, from $0.9V/V_{\mathrm{CJ}}$ to $0.77V/V_{\mathrm{CJ}}$, and there is not much difference between staggered and aligned obstacles. The reason for the uniform decline here is also because the propagation is galloping detonation (Gao et al., 2015).

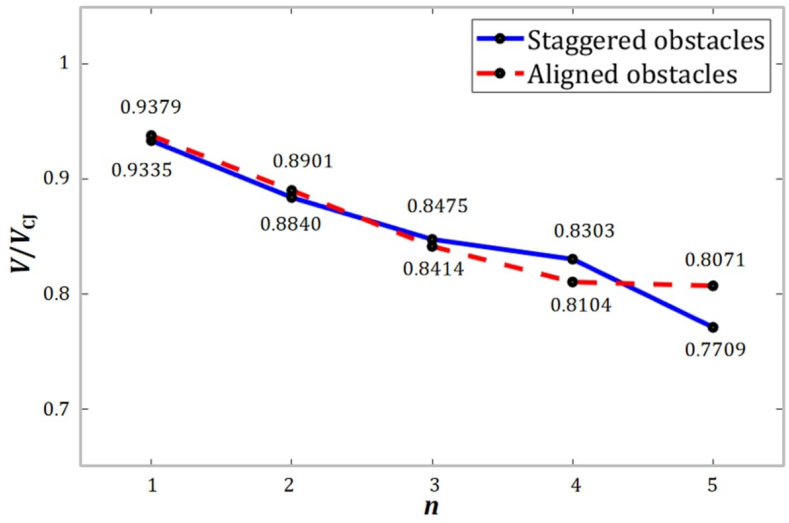

Figure 4.7: The relationship between average velocity and the roughness factor n of detonation propagation with $D_{1/2} = 300$ and heat release constant $k_{\mathrm{R}} = 4$ in staggered as well as aligned channels.

The length of each galloping detonation period in the soot foil was also measured, after which we take use of these values to plot a figure of the period over cell size Ω/λ. From this figure, we can observe that when galloping detonation occurs, except for the $n = 1$ cases, each period has an average length of 45 to 50 average cell sizes for all the cases, see Figure. 4.8.

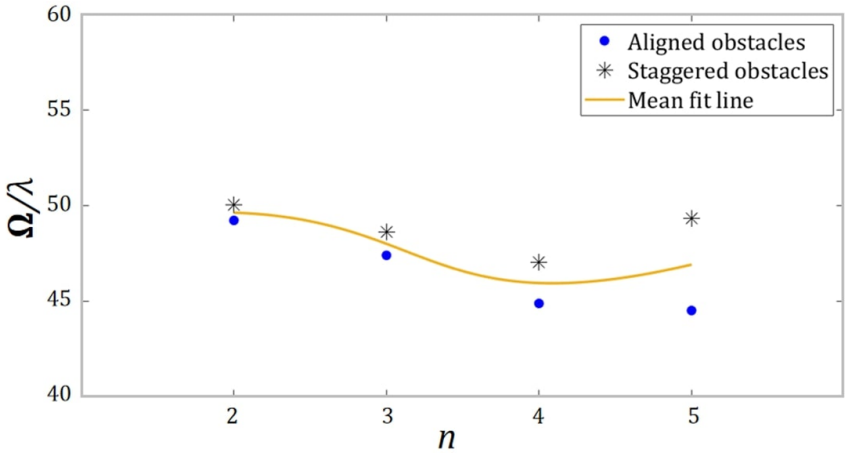

Figure 4.8: Galloping detonation period Ω over the average cell size λ for different roughness factors $n = 1, 2, 3, 4, 5$ with pre-experiential factor $k_{\mathrm{R}} = 4$ for aligned and staggered obstacles.

4.4 Probability density function comparison

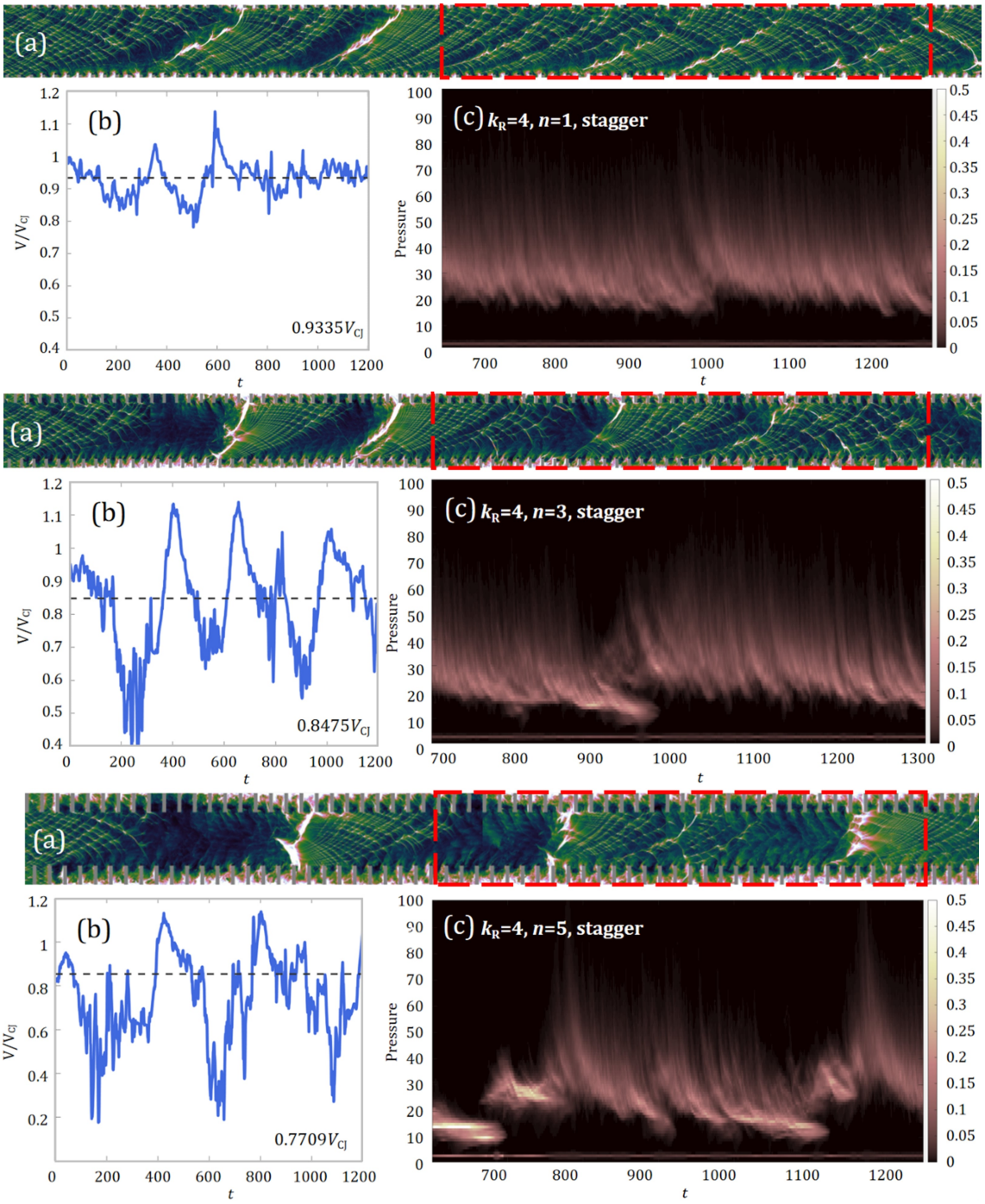

Figure 4.9: Probability density function as well as the corresponding soot foil and velocity ratio graphs for different roughness factors $n = 1, 3, 5$ with pre-experiential factor $k_{\mathrm{R}} = 4$ for staggered obstacles.

The probability density function uses the pressure values corresponding to all the cross-sectional values at each time point (that is, all the *y*-axis values at a point on the corresponding *x* coordinate axis), and draws a pressure distribution diagram at the corresponding position. The brighter the color, the more times the pressure value on the cross-section corresponding to the point appears in this value range. By carrying out the above steps for each point and combining the obtained pressure distribution maps after unifying the color bar, the distribution of the pressure values at various positions as shown in the figure can be obtained.

For the convenience of observation, we unify the soot foil, velocity ratio, and probability density function graph for observation. The probability density functions are to observe the rules of frontal shock wave pressure of detonation. We select three cases of staggered obstacle ones with roughness factors $n = 1$, 3, and 5, the following red dashed line zone is corresponding to the probability density function figures, see Figure. 4.9.

The probability density function graphs show that the peak value of pressure occurs in detonation propagation at the brightest area, which follows the soil foil graph of the re-ignition part occurs. When $n = 1$, the fading away and re-ignition parts are not obvious, so the pressure change of the generated Probability density function (PDF in short) image has no obvious color difference and is almost continuous. When $n = 3$, when the time is equal to 950, there is an obvious fading away area and the sudden color change of the pressure can also be observed in the PDF image. When $n = 5$, we can observe two fading away and re-ignition parts between the time are equal to 650 and 1250. On the PDF diagram, we can more clearly observe the pressure change when fading away, and the pressure mutation of re-ignition, as shown in the figure, the pressure of fading away is a bright line of about 15. When re-ignition occurs, our PDF image will produce a sharp spike caused by the pressure surge. And because it is a periodic cycle of galloping detonation, we can observe that the images of these two fading away and re-ignition are extremely similar.

All in all, in the numerical simulation of this paper, we found that there is almost no difference in the propagation of near-limit detonation between staggered obstacles and aligned ones, and after changing the reaction area, our simulation results showed galloping-like detonation. Similar to the previous third chapter, our detonation propagation will be affected after adding obstacles. For example, the speed will drop. After the speed drops to a certain level, fading away will occur,

that is, the decoupling of the cellular structure. Different from the previous chapter 3, because we choose a larger reaction area here, it will be easier to produce re-ignition, which is the galloping-like detonation.

Chapter 5

Conclusions

The dynamics of quasi-detonation in rough-walled tubes are investigated numerically in this work. The focus is on the effect of rough tubes with relatively small roughness, which is intended to generate only perturbations and additional instabilities to the cellular quasi-detonation. The numerical results elucidate how the wall roughness affects the cellular regularity of the quasi-detonation by comparing the case of a smooth tube. When the roughness increases (i.e., with $n = 2.5$), the decoupling between the leading front and reaction zone near the rough bottom becomes increasingly significant, and the effects are propagating and felt by the overall front, leading to the onset of failure. Besides, the length between two obstacles will also affect detonation propagation, when the recess is small enough, the influence will be tiny and no failure occurs. We also considered the impact of the obstacle arranged in aligned or staggered configurations, and the results show that the changes caused by the two are small in comparison. Using the complete simulation domain and conditions with a large chemical reaction factor k_{R} value, a galloping-like behavior of the quasi-detonation is observed, equivalent to the near-limit galloping detonation (Gao et al., 2015). This numerical study considers only the gas dynamic effects by using the ideal detonation model governed by reactive Euler's equations. When the quasi-detonation is near its limit, the effect of diffusion and turbulence should be further considered, which will provide another mechanism to sustain its propagation (Radulescu, 2018).

References

Austin, J. M. (2003). *The Role of Instability in Gaseous Detonation*. PhD thesis, California Institute of Technology, CA, USA.

Brochet, C. (1966). *Contribution à l'étude des Détonations Instables dans les Mélanges Gazeux*. l'École nationale supérieure de mécanique et d'aérotechnique, Univ. de Poitiers, Poitiers, France.

Camargo, A., Ng, H. D., Chao, J., & Lee, J. H. (2010). Propagation of near-limit gaseous detonations in small diameter tubes. *Shock Waves*, *20*(6), 499–508.

Cao, W., Gao, D., Ng, H. D., & Lee, J. H. (2019). Experimental investigation of near-limit gaseous detonations in small diameter spiral tubing. *Proceedings of the Combustion Institute*, *37*(3), 3555–3563.

Ciccarelli, G., & Cross, M. (2016). On the propagation mechanism of a detonation wave in a round tube with orifice plates. *Shock Waves*, *26*(5), 587–597.

Ciccarelli, G., & Dorofeev, S. (2008). Flame acceleration and transition to detonation in ducts. *Progress in Energy and Combustion Science*, *34*(4), 499–550.

Ciccarelli, G., Wang, Z., Lu, J., & Cross, M. (2017). Effect of orifice plate spacing on detonation propagation. *Journal of Loss Prevention in the Process Industries*, *49*, 739–744.

Cross, M., & Ciccarelli, G. (2015). DDT and detonation propagation limits in an obstacle filled tube. *Journal of Loss Prevention in the Process Industries*, *36*, 380–386.

Fickett, W., & Davis, W. C. (2000). *Detonation: Theory and Experiment.* Dover Publications, Inc., NY.

Gamezo, V. N., Desbordes, D., & Oran, E. S. (1999). Formation and evolution of two-dimensional

cellular detonations. *Combustion and Flame*, *116*(1-2), 154–165.

Gao, Y., Ng, H. D., & Lee, J. H. (2014). Minimum tube diameters for steady propagation of gaseous detonations. *Shock Waves*, *24*(4), 447–454.

Gao, Y., Ng, H. D., & Lee, J. H. (2015). Experimental characterization of galloping detonations in unstable mixtures. *Combustion and Flame*, *162*(6), 2405–2413.

Guénoche, H. (1949). The detonation and deflagration of gas mixtures. *Revue de l'Institut Français du Pétrole*, *4*, 48–69.

Hirano, T. (2002). Combustion science for safety. *Proceedings of the Combustion Institute*, *29*(1), 167–180.

Ishii, K., & Monwar, M. (2011). Detonation propagation with velocity deficits in narrow channels. *Proceedings of the Combustion Institute*, *33*(2), 2359–2366.

Jackson, S., Lee, B. J., & Shepherd, J. E. (2016). Detonation mode and frequency analysis under high loss conditions for stoichiometric propane-oxygen. *Combustion and Flame*, *167*, 24–38.

Kailasanath, K. (2003). Recent developments in the research on pulse detonation engines. *AIAA Journal*, *41*(2), 145–159.

Kellenberger, M., & Ciccarelli, G. (2020). Three-dimensional behaviour of quasi-detonations. *Combustion and Flame*, *215*, 145–156.

Kitano, S., Fukao, M., Susa, A., Tsuboi, N., Hayashi, A., & Koshi, M. (2009). Spinning detonation and velocity deficit in small diameter tubes. *Proceedings of the Combustion Institute*, *32*(2), 2355–2362.

Laffitte, P. (1923). Sur la formation de l'onde explosive. *Comptes Rendus de l'Académie des Sciences*, *176*, 1392–1394.

Lee, J. H. (1996). On the critical diameter problem. *Dynamics of Exothermicity*, 321–336.

Lee, J. H. (2008). *The Detonation Phenomenon*. Cambridge University Press, NY.

Lee, J. H., Jesuthasan, A., & Ng, H. D. (2013). Near limit behavior of the detonation velocity. *Proceedings of the Combustion Institute*, *34*(2), 1957–1963.

Liu, Y., Lee, J. H., Tan, H., & Ng, H. D. (2021). Investigation of near-limit detonation propagation in a tube with helical spiral. *Fuel*, *286*, 119384.

Ma, J. Z., Luan, M.-Y., Xia, Z.-J., Wang, J.-P., Zhang, S.-J., Yao, S.-B., & Wang, B. (2020). Recent

progress, development trends, and consideration of continuous detonation engines. *AIAA Journal*, *58*(12), 4976–5035.

Morgan, G. (2013). *The Euler Equations With a Single-step Arrhenius Reaction*. University of Cambridge, Cambridge, UK.

Nettleton, M. (2002). Recent work on gaseous detonations. *Shock Waves*, *12*(1), 3–12.

Ng, H. D., & Lee, J. H. (2008). Comments on explosion problems for hydrogen safety. *Journal of Loss Prevention in the Process Industries*, *21*(2), 136–146.

Ng, H. D., Radulescu, M. I., Higgins, A. J., Nikiforakis, N., & Lee, J. H. S. (2005). Numerical investigation of the instability for one-dimensional Chapman–Jouguet detonations with chain-branching kinetics. *Combustion Theory and Modelling*, *9*(3), 385–401.

Ng, H. D., & Zhang, F. (2012). Detonation instability. In *Shock Waves Science and Technology Library, vol. 6* (pp. 107–212). Springer Science, Heidelberg.

Radulescu, M. I. (2018). A detonation paradox: Why inviscid detonation simulations predict the incorrect trend for the role of instability in gaseous cellular detonations. *Combustion and Flame*, *195*, 151–162.

Radulescu, M. I., & Lee, J. H. S. (2002). The failure mechanism of gaseous detonations experiments in porous wall tubes. *Combustion and Flame*, *131*(1-2), 29–46.

Radulescu, M. I., Sharpe, G., Lee, J., Kiyanda, C., Higgins, A., & Hanson, R. (2005). The ignition mechanism in irregular structure gaseous detonations. *Proceedings of the Combustion Institute*, *30*(2), 1859–1867.

Ren, T., Yan, Y., Lee, J. H., Ng, H. D., Zhang, Q., & Shang, C. (2021). Velocity fluctuation and cellular structure of near-limit detonations in rough tubes. *Fuel*, *289*, 119909.

Ren, T., Yan, Y., Zhao, H., Lee, J. H., & Ng, H. D. (2020). Propagation of near-limit gaseous detonations in rough-walled tubes. *Shock Waves*, *30*(7), 769–780.

Rosato, D. A., Thornton, M., Sosa, J., Bachman, C., Goodwin, G. B., & Ahmed, K. A. (2021). Stabilized detonation for hypersonic propulsion. *Proceedings of the National Academy of Sciences*, *118*(20), e2102244118.

Roy, G. D., Frolov, S. M., Borisov, A. A., & Netzer, D. W. (2004). Pulse detonation propulsion challenges, current status, and future perspective. *Progress in Energy and Combustion Science*,

30(6), 545–672.

Shchelkin, K. (1947). Initiation of detonation in gases in rough tubes. *Technical Physics*, *17*(5), 613.

Shepherd, J. E. (2009). Detonation in gases. *Proceedings of the Combustion Institute*, *32*(1), 83–98.

Sod, G. A. (1978). A survey of several finite difference methods for systems of nonlinear hyperbolic conservation laws. *Journal of Computational Physics*, *27*(1), 1–31.

Starr, A., Lee, J. H., & Ng, H. D. (2015). Detonation limits in rough walled tubes. *Proceedings of the Combustion Institute*, *35*(2), 1989–1996.

Sun, X., & Lu, S. (2020). Effect of orifice plate on the transmission mechanism of a detonation wave in hydrogen-oxygen mixtures. *International Journal of Hydrogen Energy*, *45*(22), 12593–12603.

Teodorczyk, A., & Lee, J. (1995). Detonation attenuation by foams and wire meshes lining the walls. *Shock Waves*, *4*(4), 225–236.

Teodorczyk, A., Lee, J., & Knystautas, R. (1989). Propagation mechanism of quasi-detonations. In *Symposium (International) on Combustion* (Vol. 22, pp. 1723–1731).

Teodorczyk, A., Lee, J., & Knystautas, R. (1990). Photographic study of the structure and propagation mechanisms of quasi-detonations in rough tubes. *Progress in Astronautics and Aeronautics*, *133*, 223–240.

Toro, E. F. (2013). *Riemann Solvers and Numerical Methods for Fluid Dynamics a Practical Introduction*. Springer Science, Heidelberg.

Van Albada, G. D., Leer, B. v., & Roberts, W. (1997). A comparative study of computational methods in cosmic gas dynamics. In *Upwind and High-Resolution Schemes* (pp. 95–103). Springer Science, Heidelberg.

Voitsekhovskii, B., Kotov, B., Mitrofanov, V., & Topchiyan, M. (1958). Optical studies of transverse detonation waves. *Izvestiia Sibirskogo otdeleniia Akademii nauk SSSR*, *9*(1), 44–50.

Wang, L.-Q., Ma, H., Shen, Z., Xue, B., Cheng, Y., & Fan, Z. (2017). Experimental investigation of methane-oxygen detonation propagation in tubes. *Applied Thermal Engineering*, *123*, 1300–1307.

Wang, L.-Q., Ma, H.-H., Deng, Y.-X., & Shen, Z.-W. (2019). On the detonation behavior of

methane-oxygen in a round tube filled with orifice plates. *Process Safety and Environmental Protection*, *121*, 263–270.

Wang, L.-Q., Ma, H.-H., Shen, Z.-W., & Chen, D.-G. (2018). Experimental study of DDT in hydrogen-methane-air mixtures in a tube filled with square orifice plates. *Process Safety and Environmental Protection*, *116*, 228–234.

Wola'nski, P. (2013). Detonative propulsion. *Proceedings of the Combustion Institute*, *34*(1), 125–158.

Xiao, Q., & Radulescu, M. I. (2020). Role of instability on the limits of laterally strained detonation waves. *Combustion and Flame*, *220*, 410–428.

Yan, C., Ng, H. D., & Mi, X. (2022). A numerical study on the influence of increased instability of quasi-detonation on the critical tube diameter phenomenon. *Proceedings of the Combustion Institute*, in press (https://doi.org/10.1016/j.proci.2022.11.007).

Yuan, X., Yan, C., Zhou, J., & Ng, H. (2021). Computational study of gaseous cellular detonation diffraction and re-initiation by small obstacle induced perturbations. *Physics of Fluids*, *33*(4), 047115.

Zhang, B. (2016). The influence of wall roughness on detonation limits in hydrogen–oxygen mixture. *Combustion and Flame*, *169*, 333–339.

Zhang, B., Liu, H., & Li, Y. (2019). The effect of instability of detonation on the propagation modes near the limits in typical combustible mixtures. *Fuel*, *253*, 305–310.

Zhang, B., Liu, H., & Wang, C. (2017). On the detonation propagation behavior in hydrogen-oxygen mixture under the effect of spiral obstacles. *International Journal of Hydrogen Energy*, *42*(33), 21392–21402.

Zhang, B., Liu, H., & Yan, B. (2019). Investigation on the detonation propagation limit criterion for methane-oxygen mixtures in tubes with different scales. *Fuel*, *239*, 617–622.

Zhang, B., Liu, H., Yan, B., & Ng, H. D. (2020). Experimental study of detonation limits in methane-oxygen mixtures determining tube scale and initial pressure effects. *Fuel*, *259*, 116220.